

First light for the GRAVITY+ Adaptive Optics: extreme adaptive optics for the Very Large Telescope Interferometer

GRAVITY+ Collaboration* R. Abuter⁸, F. Allouche^{23, 9}, C. Bailet²³, M. Benisty³, A. Berdeu^{2, 9}, J.-P. Berger⁵, P. Berio²³, A. Bigioli²⁰, C. Blanchard², O. Boebion²³, H. Bonnet⁸, G. Bourdarot^{1, 9}, P. Bourget⁹, W. Brandner³, J. Brulé², P. Burgos⁹, M. Carbillet²³, C. Correia^{7, 12}, B. Courtney Barrer^{9, 25}, S. Curaba⁵, R. Davies¹, D. Defrère²⁰, A. Delboulbé⁵, F. Delplancke⁸, R. Dembet², A. Drescher¹, N. Dubost⁹, A. Eckart^{4, 14}, C. Édouard², F. Eisenhauer¹, L. Esteras Otal⁸, M. Fabricius¹, H. Feuchtgruber¹, P. Fédou², G. Finger¹, N.M. Förster Schreiber¹, R. Frahm⁸, E. Garcia⁸, P. Garcia^{7, 12}, R. Garcia Lopez^{21, 26}, R. Genzel^{1, 11}, J.P. Gil⁹, S. Gillessen¹, T. Gomes^{7, 12}, F. Gonté⁸, V. Gopinath¹, C. Gouvret²³, J. Graf¹, P. Guajardo⁹, S. Guieu⁵, W. Hackenberg⁸, M. Hartl¹, X. Haubois⁹, F. Haußmann¹, T. Henning³, P. Hibon⁹, S. Höning¹⁷, M. Horrobin⁴, M. Houllé²³, N. Hubin⁸, I. Ibn Taieb², L. Jochum⁹, L. Jocou⁵, A. Jost⁸, J. Kammerer⁸, L. Karl⁸, A. Kaufer⁹, P. Kern⁵, P. Kervella^{2, 27}, J. Kolb⁸, H. Korhonen³, L. Kreidberg³, P. Krempl⁸, S. Lacour², S. Lagarde²³, O. Lai²³, V. Lapeyrère², R. Laugier²⁰, V. Leal⁵, J.-B. Le Bouquin⁵, J. Leftley^{23, 17}, P. Léna², B. Lopez²³, D. Lutz¹, Y. Magnard⁵, F. Mang^{1, 13}, A. Marcotto²³, D. Maurel⁵, A. Mérand⁸, F. Millour^{23, 9}, M. Montarges², N. More¹, N. Morujão^{7, 12}, T. Moulin⁵, H. Nowacki⁵, M. Nowak^{15, 2}, S. Oberti⁸, T. Ott¹, L. Pallanca⁹, F. Patru²³, T. Paumard², K. Perraut⁵, G. Perrin², P. O. Petrucci⁵, R. Petrov²³, O. Pfuhl⁸, N. Pourré⁵, S. Rabien¹, C. Rau¹, M. Riquelme⁸, S. Robbe-Dubois²³, S. Rochat⁵, M. Salman²⁰, J. Sánchez-Bermúdez²², J. Schubert¹, J. Scigliuto²³, P. Shchekaturov⁸, N. Schuhler⁹, J. Shangguan^{28, 1}, T. Shimizu¹, S. Scheithauer³, C. Soenke⁸, F. Soulez²⁴, E. Stadler¹⁹, J. Stadler²⁰, C. Straubmeier⁴, E. Sturm¹, M. Subroweit⁴, C. Sykes¹⁷, L.J. Tacconi¹, K.R.W. Tristram⁹, S. Uysal¹, S. von Fellenberg^{1, 14}, F. Widmann¹, E. Wiprecht¹, E. Wiezorek¹, J. Woillez⁸, S. Yazici¹, and G. Zins⁸

(Affiliations can be found after the references)

Received: 26 May, 2025, 2025; accepted: 24 September, 2025

ABSTRACT

GRAVITY+ improves by orders of magnitude the sensitivity, sky-coverage, and contrast of the Very Large Telescope Interferometer (VLTI). A central part of this project is the development of Gravity Plus Adaptive Optics (GPAO), a dedicated high-order and laser-guide star adaptive optics (AO) system for VLTI. GPAO consists of four state-of-the-art AO systems that equip all 8m class Unit Telescopes (UTs) for the wavefront correction of the VLTI instruments. It offers both visible and infrared natural guide star (NGS) and laser guide star (LGS) operations. The paper presents the design, operations, and performances of GPAO. We illustrate the improvement brought by GPAO with interferometric observations obtained during the commissioning of the NGS mode at the end of 2024. These science results include the first optical interferometry observations of a redshift $z \sim 4$ quasar, the spectroscopy of a cool brown-dwarf with magnitude $K \sim 21.0$, the first observations of a Class I young star with GRAVITY, and the first sub-micro arcsecond differential astrometry in the optical. Together with the entire GRAVITY+ project, the implementation of GPAO is a true paradigm shift for observing the optical Universe at very high angular resolution.

Key words. Instrumentation: adaptive optics – Instrumentation: interferometers – Instrumentation: high angular resolution – Galaxies: quasars: supermassive black hole – Planets: exoplanets

1. Introduction

Adaptive optics (AO) was identified early on as a prerequisite for interferometry on large telescopes, in order to work with apertures larger than the Fried diameter and increase the coherent volume for interferometry (Léna 1988; Eisenhauer et al. 2023). The use of AO directly results in a sensitivity improvement of $\propto D^4$ for diffraction-limited interferometric observations, compared to $\propto D^{1/3}$ in the case of seeing-limited observations (Eisenhauer et al. 2023). As such, the use of AO has been rapidly proposed to correct the wavefront before interferometric combination in place of multi-speckle interferometry (Roddier 1981), as well as to correct the coupling of light into single-mode fibers (Shaklan & Roddier 1988) for infrared

* GRAVITY+ is developed in a collaboration by the Max Planck Institute for extraterrestrial Physics, the Institute National des Sciences de l'Univers du CNRS (INSU) with its institutes LIRA / Paris Observatory-PSL, IPAG / Grenoble Observatory, Lagrange / Côte d'Azur Observatory and CRAL / Lyon Observatory, the Max Planck Institute for Astronomy, the University of Cologne, the CENTRA - Centro de Astrofísica e Gravitação, the University of Southampton, the Katholieke Universiteit Leuven, University College Dublin, Universidad Nacional Autónoma de México and the European Southern Observatory.

Corresponding authors: J.-B. Le Bouquin (email: jean-baptiste.lebouquin@univ-grenoble-alpes.fr), G. Bourdarot (email: bourdarot@mpe.mpg.de), A. Berdeu (email: anthony.berdeu@obspm.fr)

interferometry.

In this paper, we present the Gravity Plus Adaptive Optics (GPAO) system, the new AO system of the Very Large Telescope Interferometer (VLTI), and its first on-sky observations. Section 2 introduces the instrumental context at the VLTI and the rationale for a new system. Section 3 details the design choices and the implementation of GPAO in the VLTI 8 m telescopes. Section 4 presents the operation and the performance of AO. Section 5 illustrates the new science enabled by presenting the first interferometric observations obtained with the natural guide star mode of GPAO that were commissioned at the end of 2024. The laser-assisted mode will be commissioned at the end of 2025 and its on-sky results will be presented in a later paper. All acronyms used throughout this paper are described in Appendix H.

2. Context at the VLTI and GRAVITY+

2.1. Optical-Infrared interferometry with large telescopes and adaptive optics:

The role of AO for the 8m-class telescopes on the Very Large Telescope Interferometer (VLTI) was emphasized from its initial design: "The largest gains in sensitivity of the VLTI will come from the incorporation of AO which will make the telescope diffraction limited at 2 μm " (Beckers 1990). Therefore, a dedicated AO facility was implemented at VLTI from its early start with the Multi-Application Curvature Adaptive Optics (MACAO, Arsenault et al. 2003). The emphasis was made on multipurpose applications, with a trade-off between limiting magnitude and wavefront quality in the absence of laser guide stars and technological limitations at the time. The VLTI was later upgraded with an infrared AO, the GRAVITY Coudé Infrared Adaptive Optics (CIAO, Scheithauer et al. 2016), to provide AO for the extremely red Galactic Center region.

The next step on large telescopes is the development of an AO facility enabling both natural guide star (NGS) and laser guide star (LGS) operations. Unlike small telescopes, for which the limiting magnitude is set by the number of photons available for fringe-tracking, the limiting magnitude for large telescopes is constrained by the AO system (Eisenhauer et al. 2023). This originates from the fact that the number of photons available for fringe-tracking increases with the collecting area, while for AO this number is set by the number of photons per turbulence cell, whatever the size of the telescope. For a telescope size larger than the Fried parameter, the limiting magnitude is thus independent of the size of the telescope. This limitation is lifted with LGS AO, where the high-order correction is done on an artificial star. The limiting magnitude in this case is set by the tip-tilt correction, which requires a nearby star in the isokinetic patch. This magnitude is comparable to the fringe-tracking limiting magnitude. Therefore, an LGS AO system is the only way to reach the ultimate interferometric sensitivity of an array of large apertures. Moreover, when LGS operations are available to cover the faint end, the NGS operations can be optimized for peak performances on the bright end, overcoming the trade-off between limiting magnitude and wavefront quality.

2.2. GRAVITY overview

The GRAVITY instrument (GRAVITY Collaboration et al. 2017) is a four beam interferometric instrument, offering milli-arcsecond (mas) resolution imaging for objects as faint as $m_K > 20$, together with 30 – 100 micro-arcsecond (μas) narrow-angle

astrometry, and micro-arcsecond spectro-astrometry capabilities in the K-band (2.0–2.4 μm). The instrument allows one to perform phase-referenced observations by using two objects that can be observed simultaneously, one for the Fringe-Tracker (FT) channel that compensates in real-time for the atmospheric piston, and one for the science channel (SC) for long exposures. GRAVITY has delivered ground-breaking results, from the experimental test of General Relativity in the Galactic Center and the study of the environment of the Sgr A* black-hole down to the innermost circular orbit scales (GRAVITY Collaboration et al. 2018a,b, 2019a, 2020a, 2022), to the first spatially resolved observations of a broad-line region (BLR) in an active galactic nucleus (AGN, GRAVITY Collaboration et al. 2018c), the first detection and characterization of exoplanets using interferometry (GRAVITY Collaboration et al. 2019b, 2020c; Nowak et al. 2020; Lacour et al. 2021), the first resolved image of a gravitational microlens (Dong et al. 2019), and spatially-resolved surveys of the inner disks of young stars and their magnetospheric accretion regions (GRAVITY Collaboration et al. 2019c, 2020b, 2021, 2023, 2024b).

2.3. From GRAVITY to GRAVITY+

The goal of the GRAVITY+ project is to increase the sensitivity, sky-coverage, and high-contrast capability of GRAVITY and of the VLTI infrastructure by several orders of magnitude (Gravity+ Collaboration et al. 2022), with the primary objectives being to (1) measure the dynamical masses of Super Massive Black Holes in AGNs across Cosmic Time by resolving their BLR (2) characterize the physics of exoplanets at astronomical-unit separations by directly detecting their continuum emission or albedo and spectral signature, and (3) constrain the spin of SgrA* in the Galactic Center by unveiling and following faint objects on close-in orbit within the potential well of the black hole.

The GRAVITY+ project was first presented in 2019 (Eisenhauer 2019; Mérand & Leibundgut 2019). In 2021, its phased implementation started with the GRAVITY Wide mode (hereafter G-Wide, GRAVITY+ Collaboration et al. 2022), which enabled for the first time wide-field observations with GRAVITY. This upgrade leverages the dual feed capability baked into VLTI since its conception and developed by the former PRIMA project (Woillez et al. 2014). Before this upgrade, the maximum FT-SC separation was limited to 2 arcseconds on the UTs and 4 arcsecond on the ATs. This requirement is overcome by G-Wide, which enlarges the maximum separation between the FT and SC to 30 arcseconds (both for ATs and UTs) by using the star separator (STS) at the Coudé focus of the telescopes (Nijenhuis & Giesen 2005). The much larger area in which to pick up a bright star suitable for fringe-tracking is virtually limited by the isopistonic angle, thus increasing the field-of-view and the sample of observable objects. This instrumental upgrade was necessary for the observations of faint sources with interferometry, in particular extragalactic sources, which are too faint to allow for fringe-tracking. The G-Wide upgrade enabled the dynamical mass up of a super massive black hole (SMBH) to be measured to a redshift $z \sim 2$ for the first time (Abuter et al. 2024).

The implementation of GRAVITY+ continued with the completion of an upgrade of the GRAVITY metrology, the introduction of the so-called FAINT mode in order to remove the noise of the metrology laser (Widmann et al. 2022), an improvement of global throughput by combining the beam compressor and the differential delay lines in the VLTI laboratory (Fabricius et al. 2024), and the upgrade of the GRAVITY fringe-tracker (Nowak et al. 2024b). These upgrades will soon be complemented by the

installation of high-precision injection optics for astrometry in GRAVITY and a high-resolution grism $R \sim 15,000$ (Gravity+ Collaboration et al. 2022), and possibly an improved vibration control for VLTI (Bigioli et al. 2022; Laugier et al. 2024).

The deployment of GRAVITY+ has put the system in a situation where most cases are limited by the performance of the MACAO system. On the one hand, observations of faint objects with the wide-field mode are in practice limited to a handful of targets because the limiting magnitude of the fringe-tracker ($m_K \lesssim 12$) corresponds to objects that are too faint in the visible for decent AO correction ($m_V \lesssim 13$). On the other hand, observations of ever more contrasted exoplanets require a higher-order AO correction to maximize the collected flux of the planet, while reducing the speckle and photon noises coming from the nearby bright star (Lacour 2023). As explained above in this introduction, these barriers can only be lifted by the deployment of an AO facility that enables both NGS and LGS operations. This is exactly the purpose of the GPAO system, developed in the framework of the GRAVITY+ project.

3. Instrument design

3.1. General design guidelines and trade-offs

The analysis resulting in the final design of GPAO inherits from: (I) the Enhanced Resolution Imager and Spectrograph (ERIS, Davies et al. 2023) for the overall error budget, the implementation of the new wavefront sensors, and the Standard Platform for Adaptive optics Real Time Applications (SPARTA) framework for the Real Time Computer (RTC), (II) the Adaptive Optics Facility, the GRound layer Adaptive optics Assisted by Lasers and the Ground Atmospheric Layer Adaptive Corrector for Spectroscopic Imaging (AOF, GRAAL and GALACSI, Ströbele et al. 2006) for the operational experience at Paranal observatory (Pauquie et al. 2016; Hartke et al. 2020), especially with the LGS, (III) CIAO (Kendrew et al. 2012) for the infrared wavefront sensor hardware and its operation, and (IV) the New Adaptive Optics Module for Interferometry (NAOMI, Woillez et al. 2019) for the overall interface concept with VLTI, as well as the emphasis on automatic and reliable operations. On the other hand, Appendix A lists the differences between GPAO and these projects that have a significant impact on the design.

3.1.1. ALPAO 43x43 deformable mirror

The size of the deformable surface is imposed by the design of the VLTI Coudé train (see Fig. 1), where the pupil defined by the secondary mirror (M2) is reimaged on the mirror number 8 (M8) with a size of 98×101 mm. The voice coil technology from ALPAO¹ was identified as the most cost-effective solution to achieve the required stroke ($>15 \mu\text{m}$ peak-to-peak wavefront for 3×3 actuators), speed (>800 Hz) and the necessary pupil size (101 mm).

The actuator density corresponds to an extreme-AO system (effective pitch of about 20 cm on-sky), because (1) there is no trade-off between a high-order system and a sensitive system thanks to the LGS-assisted mode, (2) there is no trade-off between the number of actuators and the stroke or the speed in the ALPAO technology, and (3) it enables shorter wavelengths that, even if outside the immediate scope of GRAVITY+, are of interest for the long-term future of VLTI.

A prototype deformable mirror (DM) was used from October 2022 to August 2023. Two main conclusions could be drawn. First, the ALPAO standard technology (polymer springs) satisfies the requirement in term of actuator gain stability and homogeneity. Considering the risk inherent to any new technology, the mitigation plan of using innovative metallic springs for the final DMs was dropped. Secondly, the edges of the pupil were poorly controlled by the 41×41 2.5 mm pattern. The design was thus upgraded to 43×43 with a custom pitch of 2.62 mm. This is the design for the final six GPAO DMs (four in operation and two spares).

3.1.2. OCAM2 camera and frame grabber

The Spectro-Polarimetric High contrast imager for Exoplanets REsearch (SPHERE, Beuzit et al. 2019), GALACSI, GRAAL and ERIS use a camera internally developed by the European Southern Observatory ESO based on the EMCCD220 chip from e2v. GPAO instead uses the commercial OCAM2 camera from First Light Imaging² based on the same chip, with comparable performances (sub-electron readout noise, >1 kHz full frame rate). However, the video protocol of this camera (Camera Link Full) is not supported in the ESO standard, and the physical distance between the wavefront sensor (WFS) location and the RTC cabinets renders a conversion to optical fiber necessary. GPAO uses a commercially available frame grabber in order to execute the protocol and media conversions (see Sec. 3.2.5). The stability of the data stream and the additional latency in the frame grabber were validated with the first camera, delivered in 2021.

3.1.3. Shack Hartmann versus pyramid wavefront sensors

The Pyramid sensor may appear as a more promising solution than a Shack-Hartmann (SH) for GPAO because of its improved sensitivity to the low orders, which are critical to inject inside a single-mode fiber or reach high contrast at a small inner working angle. Moreover, assuming a detector with sub-electron readout noise, a Pyramid sensor allows the number of measured modes to be reduced without modifying the optical setup (e.g., when the NGS WFS is used as a low-order sensor in LGS mode).

For the NGS VIS WFS, the Pyramid sensor has been discarded for three reasons. First, the correction of the large amplitude non-common path aberrations (NCPA) created by the downstream VLTI optical train challenges the linearity of the Pyramid sensor. Second, the selected DM technology suffers from gain instabilities and creep (with typical timescale of several seconds to days). We adopted the precautionary principle to associate this possibly nonlinear actuator with a linear, reproducible sensor so that a recalibration is always possible. And third, the development in the RTC to support the Pyramid with respect to the baseline ERIS algorithms were in contradiction with the timeline of the GPAO project. We also considered the lack of operational experience with the Pyramid sensor within ESO, while the SH had been operated with a high level of reliability for many years, which is critical for a complex system like VLTI.

For the LGS WFS, the Pyramid sensor has been discarded because the critical low orders are sensed by the NGS sensor anyway. Furthermore the behavior of a Pyramid WFS with the LGS elongated spot is not yet completely understood.

¹ www.alpao.fr

² www.first-light-imaging.com

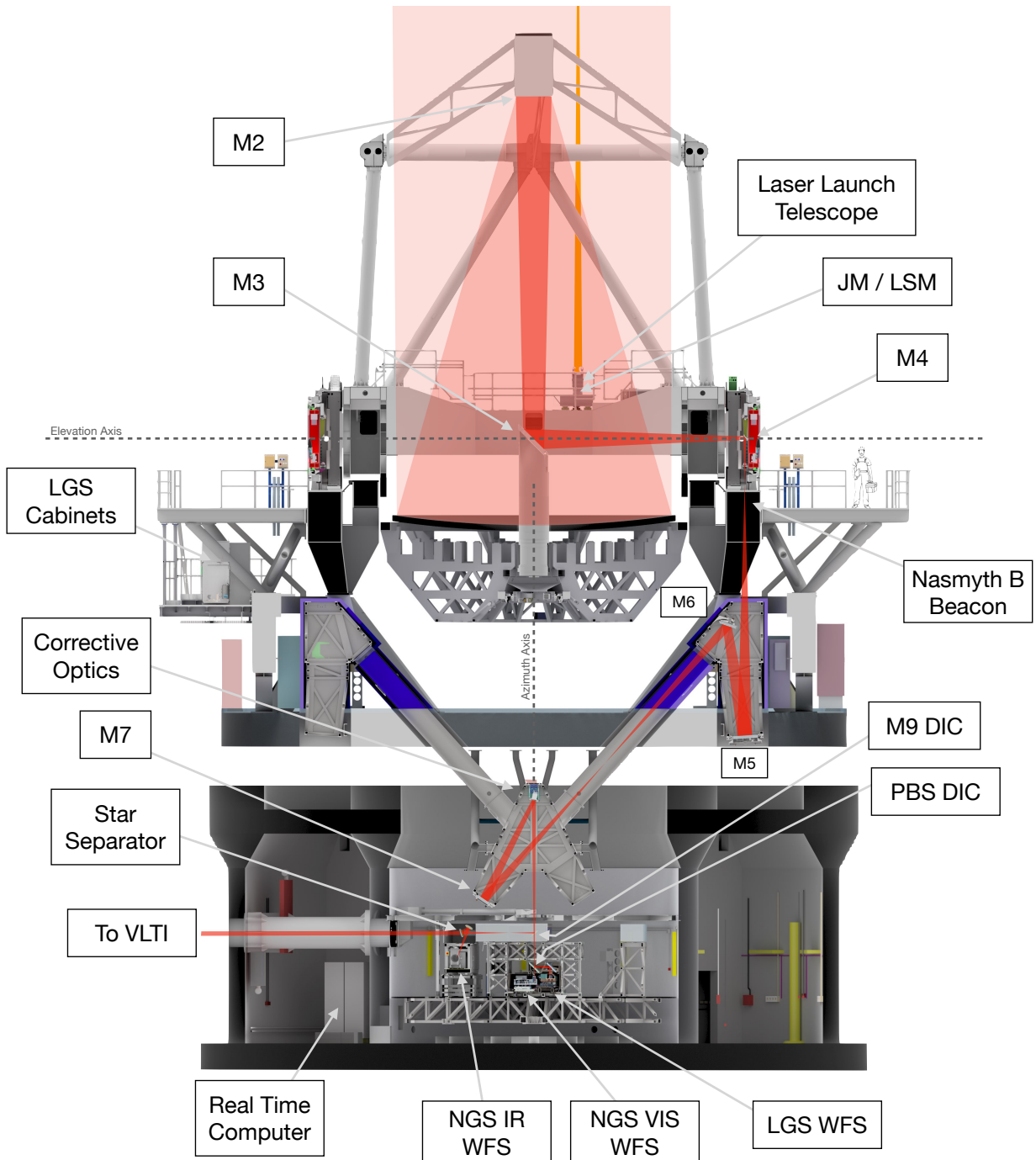


Fig. 1. Location of the subsystems of GPOAO within the structure of the unit telescope. The beam of light is represented in light red, from the vertical incidence on M1 down to the exit toward the VLTI tunnel. Although they are not formally GPOAO subsystems, the location of the M2 mirror, the elevation and azimuth axes, the Nasmyth beacon, the mirrors of the Coudé train, the M9 dichroic, and the star separator are also highlighted because of their particular importance for GPOAO.

3.1.4. Number of measured modes

The philosophy motivating the design is the following: the GPOAO NGS mode is optimized for robust peak performances on bright stars, the GPOAO LGS mode is optimized for robust performances toward the faint end. On the one hand, considering the DM characteristics, the maximum useful repetition rate of the AO loop is 2 kHz, which is matched by the OCAM2 camera in full frame. Therefore, there is no trade-off between the number of pixels to read and the speed. On the other hand, the RTC prototyping activity predicted a maximum loop rate of 2 kHz for

an ERIS-like system ($\approx 40 \times 40$ sensing, ≈ 1200 actuators). So, there was no trade-off between the number of sub-apertures and the speed. Consequently, the baseline design for the GPOAO NGS mode is to control up to 900 modes with a 40×40 SH.

The LGS WFS controls up to 500 modes with a 30×30 SH. With respect to a 40×40 , the 30×30 provides improved robustness against situation of low-sodium density. A 20×20 , while obviously even more robust to lower flux return, would have significantly degraded performances in the case of average

seeing and hampered the perspective of shorter wavelengths at the VLTI.

3.1.5. Piston-free operation

An AO system for an interferometer will provide a piston-free correction. There are subtleties in this definition (e.g., mean defined over pupil or pupil apodized by the single mode fiber of the instrument) but the analysis is identical at first order. The piston properties of the ALPAO mirror technology were investigated by the NAOMI project (Woillez et al. 2019). First, this study demonstrated that it is possible to construct a piston-free modal basis, without the need for a position sensor (Le Bouquin et al. 2018). Secondly, this study showed that the stroke of piston-free modes is only slightly reduced compared to their optimal counter-part including piston, and only for low-order radially symmetric modes (focus, spherical, and higher order spherical). Altogether, we concluded that the classical requirements on DM manufacturing (stability, calibrability) and on the RTC design (modal control) fit the need of GPAO.

3.1.6. Integration of CIAO

CIAO is the 9×9 SH WFS providing off-axis infrared (IR) wavefront sensing for the observations of the Galactic Center with GRAVITY (Scheithauer et al. 2016). It is fed by the second beam getting out of the star separator (STS) at the Coudé focus of the UTs. The CIAO RTC is built on the SPARTA-light platform. It controls 40 modes, to match the degree of freedom of the MACAO deformable mirror.

In order to maintain the IR wavefront sensing at VLTI, the CIAO hardware is fully integrated as an additional sensor of the GPAO system. The opto-mechanical hardware and the local controllers remained unmodified. The CIAO RTC, the workstations and the high level control software have been decommissioned. This choice was motivated for its opportunity of combining the CIAO infrared sensor with the new LGS sensor for the Galactic Center. The nearby GCIRS7 star ($m_K=6.5$ at $6''$) is used for sensing the tip-tilt and focus (with the possibility for up to 44 modes) in the IR while the LGS WFS senses the higher order modes. Without IR sensing, the closest visible star is fainter and further away ($m_V=14$ at $15''$). This approach also strongly simplifies the operations by merging all sensors (VIS, IR) into a common AO system for VLTI/UT.

3.1.7. Zonal versus modal control

Fundamentally, the control in GPAO is modal, in the sense that the control space is determined by a subset of predefined Karhunen-Loëve modes (KL, see Sect. 3.4.1), and not by a subset of the eigenvectors of the WFS+DM system. This classical approach in modern AO delivers improved performances by focusing on the modes with highest turbulence power. The control can be "explicitly modal" (a different temporal filter is applied on each mode) or "implicitly modal" (the modal space is defined by the row-space of the control matrix, complement of its kernel, and the same temporal filter is applied to all elements of the command vector). Systems exist in both approaches.

The explicitly modal approach allows the temporal filters to be tuned differently on each mode, for instance to reject known vibrations on a given mode, or to implement large leaks on high-order modes. But its implementation in SPARTA suffers from an increased latency because of a second, post-filter matrix mul-

tiplication (modes to DM commands). Considering the risk on the latency and the necessary development time, it was decided to implement the high-order controllers of GPAO as implicitly modal. Ultimately, modal leaks could still be implemented in these implicitly modal controllers, as described in Appendix D.

3.1.8. Software derotations

GPAO is unusual in the number of rotations inside the system. The photometric pupil and its spiders (M2), as well as the Jitter mirror of the Laser Launch Telescope, rotate with respect to the WFS by the angle *Azimuth - Elevation*, which is constantly changing while the telescope is tracking. The DM rotates with respect to the WFS by the *Azimuth* angle, which is also constantly changing. We decided to avoid any mechanical derotation inside the WFS, meaning that both the photometric pupil and the DM pattern rotate on the WFS. This strategy rigidifies the entire ensemble of M9 + Plano Beam Splitter (PBS) + WFSs + STS + VLTI into a common, nonrotating frame (see Fig. 1 and discussion in Sect. 3.1.8 and Fig. 2). Doing so significantly simplifies the geometrical modeling of the instrument and the management of the NCPA.

Consequently, GPAO has to implement a numerical derotation. The strategy implemented in the former CIAO (measuring the DM/WFS interaction matrix at many Azimuth angles, defining a subset of system modes properly seen at all angles, and precomputing a bank of control matrices) would be extremely time-consuming in calibration considering the number of modes in GPAO and the increased sensitivity to the system angle. The strategy implemented in NAOMI (rotating the controlled Zernikes) is not possible in GPAO because the control space (KL modes) does not define a rotation operator. Instead, GPAO relies on pseudo-synthetic interaction matrix (PSIM, see Sect. 3.4.4) created with a geometric model of the instrument. The angle between the DM and the WFS is one of the parameters of this geometric model. The control matrix is recomputed on-the-fly based on the actual Azimuth angle. The highest update rates (5 s) allow the meridian to be crossed at a zenithal distance of 5 deg while controlling 900 KL modes.

3.1.9. Patrol fields

For the NGS WFS, it makes sense for the patrol field to be larger than the isokinetic angle in the longest wavelength used by VLTI (10 μm), in good seeing conditions. In practice, this means covering the entire 1 arcmin (radius) telecentric field of view at the Coudé focus of the UTs.

For the LGS WFS, we also decided to patrol the entire Coudé field of view. This made it possible to put the LGS star on any of the two objects transmitted to VLTI (one being the fringe-tracking star, the other being the science object). It also allows small pointing offsets to be added to the LGS spot, fixed in pupil orientation, as a mitigation to potential Rayleigh contamination.

3.2. Description of subsystems

3.2.1. Implementation in the Unit Telescopes

Figure 1 highlights the location of the main subsystems of GPAO within the structure of the Unit Telescopes. Relevant optical elements are the secondary mirror M2 that defines the aperture stop of the telescope, the DM located in M8 and conjugated with M2, the dichroic beam splitter M9 that reflects the infrared part $> 1 \mu\text{m}$ for the VLTI/STS/CIAO and transmits the optical light

Table 1. Parameters of GPAO wavefront sensors associated with their corresponding AO mode.

Parameter	LGS	NGS VIS HO	NGS VIS LO	NGS IR HO	NGS IR LO
Camera	OCAM2	OCAM2		Saphira	
Nb. of pixel read	240 × 240	240 × 240		72 × 72	
Pattern of subap	30 × 30	40 × 40	4 × 4	9 × 9	
Nb. of subap	704	1240	12	68	
Plate scale ["/pix]	0.71	0.42	0.21	0.51	
Frame rate [Hz]	1000	1000,500,250,100	500,250,100	1000,500,200,100	500,200,100
Controlled KL modes	4-500	500,200	3	50	3
Modal controller	implicit	implicit	explicit	implicit	explicit
is active in mode:					
NGS_VIS		✓			
NGS_IR				✓	
LGS_VIS	✓		✓		
LGS_IR	✓				✓

Notes. In terms of hardware, the NGS VIS HO/LO wavefront sensors only differ by the setting of the NHILO lenslet. In terms of hardware, the NGS IR HO/LO wavefront sensors are identical.

to the visible and laser WFSs, and the telecentric doublet lens located just below M9 in the transmitted Coudé focus. This lens acts as a (quasi) field lens and provides a telecentric field plane of 1.5 arcmin at f/47, the so called patrol field. The M9 dichroic being in a convergent beam close to focus, it generates field-dependent aberrations and pupil distortions in the transmitted beam.

3.2.2. Wavefront sensors

The new wavefront sensors of GPAO enable NGS VIS and LGS operations (Bourdarot et al. 2024). Their design is based on the AO module of ERIS (Riccardi et al. 2018), adapted from a f/13.6 beam to a f/47 beam. The WFS are located at the Coudé, below the VLTI STS and M9 dichroic (Fig. 1). Inside the WFS unit, the Periscope Beam Splitter (PBS, a plano-parallel dichroic) reflects the light of the sodium laser line around 589.195 nm toward the LGS WFS, and transmits the broad band natural light (600 – 1000 nm) toward the NGS VIS WFS. Each of the two wavefront sensors are installed on a translation XY-stage that cover the full patrol field of 2 arcmin. The parameters of the WFS corresponding to the respective AO modes are indicated in Table 1.

NGS VIS WFS The natural guide star visible WFS is a Shack-Hartmann that can be configured either as a high-order (HO, 40 × 40) sensor or as a low-order (LO, 4 × 4) sensor. It is composed of eight main subsystems. (i) The atmospheric dispersion compensator (ADC) is composed of a pair of Amici prisms, and designed for a maximum zenith angle of 70°. (ii) The technical charge couple device (TCCD), uses the blue part of the spectrum < 400 – 570 nm (R > 95%) reflected from an internal dichroic (DCR). It allows either the pupil or the field to be imaged using a moving lens, and can be used as an acquisition camera with 20" field of view. (iii) The NGS pupil steering mirror (NPSM) adjusts the position of the pupil with a piezo-driven mirror, located close to an intermediate image plane with f/20. (iv) The NGS field diaphragm (NDIA), located in the image plane, limits the field-of-view of the subapertures to avoid cross-contamination. (v) The filter wheel is a set of neutral densities

(1/10 and 1/100), a He-Ne notch filter, a Sodium notch filter, and a long-pass > 800 nm filter for best performances on bright stars. (vi) The NGS derotator (NROT), made of FK5 prism. In normal operation, this device is fixed. (vii) The HO/LO translation stage switches between either the HO or LO lenslet arrays. (viii) The OCAM2 camera measures the output spots, with a full detector size of 240 × 240 pixels. The electron-multiplication (EM) gain enabled by the EMCCD ranges from 1 to 1000. The overall bandpass of this wavefront sensor, including the Coudé train, matches the G_{RP} bandpass (Gaia Collaboration et al. 2021).

LGS WFS The laser guide star WFS is a Shack-Hartmann with a fixed configuration. The beam is converted from f/47 to f/12 in order to adjust for the large focusing range. It is composed of 4 main elements. (i) The laser focus control stage (LFOC), which allows the focus to be adjusted from 80 km to infinity. (ii) The LGS derotator (LROT) is kept fixed in normal operation. (iii) The LGS pupil steering mirror (LPSM), located close to the image plane, steers the pupil based on the same principle as in the NGS. (iv) The 30 × 30 lenslet array is fixed inside the OCAM2 camera. When observing in LGS mode, the NGS and LGS camera are synchronized by a physical link that distributes a common clock.

Calibration Unit The calibration unit of the WFS subsystem consists of two multi-mode fibers located in the respective focal point of the NGS VIS and of the LGS wavefront sensors. The fibers are fed with a broadband halogen lamp that covers the optical/near-IR spectrum (400 – 1000 nm). The calibration unit is moved in and out of the optical path by a linear translation stage. The NGS IR wavefront sensor does not have a calibration unit.

3.2.3. Corrective optics and deformable mirror

The corrective optics (CO) assembly is located in the M8 position of the UT. It is composed of a motorized gimbal tip-tilt mount that hosts the deformable mirror itself.

The ALPAO Deformable Mirror (DM) features 1432 actuators on a square 2.62 mm pitch pattern. The stroke of pushing a group of 3×3 actuators is typically 20 μm peak-to-peak wavefront, with respect to the zero position (that is: this stroke is achievable in both directions). The first resonance is 1000 Hz. The DM is controlled by two standard Drive Electronics of ALPAO, each featuring two Ethernet connections. One is dedicated to house keeping and monitoring, and the other to the high speed data link (1 Gbit/s). The DM is equipped with cooling plates on two of its lateral faces. The flow of coolant is regulated to maintain the DM internal temperature to less than 3 deg above the ambient temperature at the location of the DM.

The center of the DM (actuator 716, starting 0) is located on the Azimuth axis of the telescope with an accuracy better than 0.5 mm. The DM is mounted in a quasi-static gimbal mount (QSM) to provide a large range (2 deg-mechanical, > 2 arcmin-sky), slow tip-tilt with the vertex in the center of the DM surface. The actuation is absolutely encoded with a resolution of 10 mas-sky. This actuation serves to steer the Nasmyth Beacon anywhere in the Coudé field of the UT, and to offload the DM tip-tilt when doing calibration. When observing on sky, the QSM is kept static at the position corresponding to the optical axis of the telescope.

The electronic cabinet of the Corrective Optics is located inside the inner track of the UT to keep the distance to the DM shorter than 3 m. This cabinet embarks the two DM electronic racks (each driving ~ 700 actuators), the local controllers of the motors of the gimbal motion, and a low-latency Ethernet switch used to convert the incoming high speed and housekeeping networks (transported over fibers) into copper cables.

3.2.4. Laser guide stars

GPAO will be operated with the LGS to be installed on UT1-2-3 (Booth et al. 2024) and with LGS#1 installed on UT4 (Calia et al. 2014). The laser sources of UT1-2-3 are essentially identical to those used in the UT4 Adaptive Optics Facility (Karpov et al. 2011) and those that will be used on the ELT. The LGS laser source feeds a laser projection subunit (LPS) mounted on the side of the UT primary mirror. The LPS of UT1-2-3 are identical to those used on the ELT (Nijenhuis et al. 2024) and are comparable in performance to the one of UT4. The LPS is basically a reversed telescope equipped with a fast Jitter Mirror (JM) and a slow Laser Steering Mirror (LSM) used to control the beam direction. Each UT is equipped with its own camera-based aircraft avoidance system to prevent beam collisions with planes.

3.2.5. Real time computer

The real time computer (RTC) is made of two components. First, the hard RTC (HRTC) is responsible of the main low-latency control loop. Second, the soft RTC (SRTC) is in charge of monitoring and driving the HRTC with high level, but not real-time, tasks. GPAO reuses and improves many features of the ERIS RTC (Baruffolo et al. 2018), the AOF RTC (Kolb et al. 2012) (e.g., the real time calculations blocks) and of the NAOMI RTC (e.g., the chopping and the saturation management, and the communication with the ALPAO deformable mirrors).

HRTC The HRTC is based on the SPARTA-upgrade platform from ESO (Shchekaturov 2023), which replaces the SPARTA RTC box by a single workstation. The HRTC receives the pixels of the OCAM2 cameras via Pleora iPort CL-Ten frame grabbers in GigE-Vision (10 Gigabit Ethernet, GbE). The HRTC receives

the pixels of the NGS IR Saphira detector using the native serial front panel data port (sFPDP). It sends command to the DM using the ALPAO HSDL protocol through two 1 GbE links (one per electronic). The HRTC also sends commands to the JM and LSM mirrors in ESO MUDPI format through a 10 GbE link. The hardware chosen for the HRTC is the Dell PowerEdge R7525 server, equipped with additional Intel X710-T4 Network Interface Cards and one New Wave DV v5051 sFPDP Card. The system is configured to run as deterministic as possible (diskless, load only required interfaces, confine the kernel). It takes advantage of its multi-CPU architecture, of the principle of Interrupt Request affinity and of the NUMA architecture. The HRTC use non-blocking communications and shared memory areas to exchange intermediate results so that the data can be processed in parallel to their reception as much as possible.

SRTC The SRTC is the interface between the HRTC and the outside world. It catches the HRTC real-time stream, analyzes performance parameters, triggers alarms, and updates the matrices and references vectors. The SRTC mostly interacts with the Observation Software (OS) and its secondary loops (see Appendix C), to which it sends measurements (e.g., pupil position, mean tip-tilt), and from which it receives updates and commands (e.g., new rotation angles, trigger to recompute the control matrix, new NCPA vector). In terms of hardware, the SRTC is implemented as a standard SPARTA cluster composed of several workstations connected via a 10 GbE switch.

The SRTC implements different modules that were adapted or improved to meet GPAO needs. (i) The PSIM module implements the synthetic model of the system used to generate the control matrices (see Sect. 3.4.4). (ii) The misregistration monitor fits the PSIM parameters, either from calibration or inferred from the AO telemetry, as described by Béchet et al. (2012). (iii) The shift monitor is dedicated to lateral error estimation. It implements innovative methods (Berdeu et al. 2024a,b) with a fast and robust, but perturbative, solution for the automated acquisition, see Sect. 4.1.2, and a noninvasive approach for closed loop operations, see Sect. 3.4.5. (iv) The spot monitor uses a global inverse problem approach to robustly fits the spot parameters jointly through all the SH-WFS subapertures: spot flux, spot position, spot size in NGS, sodium layer thickness in LGS, elongation, and orientation of natural extended objects. The robustness of the approach makes it an essential tool for the automated acquisition (see star detection, star centering, magnitude estimation in Sect. 4.1.2). This module also computes the weight maps for the weighted center of gravity used on faint or extended objects. (v) The loop monitor analyzes the AO loop telemetry to compute average offloads (focus, tip-tilt) or to raise alarms (DM clips or saturation, under-illumination, over-illumination) to inform the OS which is in charge to open or not the loops. (vi) The atmosphere performance monitor estimates the atmospheric conditions (r_0 , L_0 , seeing, Strehl, ...) based on the pseudo-open loop slopes computed from the AO telemetry. It is directly inherited from AOF. A new wind speed estimator has been integrated as well, based on a frozen flow multilayer model. (vii) Finally, the pupil monitor follows the lateral position of the photometric pupil, with the possibility to finely fit the pupil magnification and relative angle.

3.2.6. Control software

The control software of GPAO is independent for each telescope, both in hardware and software. Each GPAO has two workstations

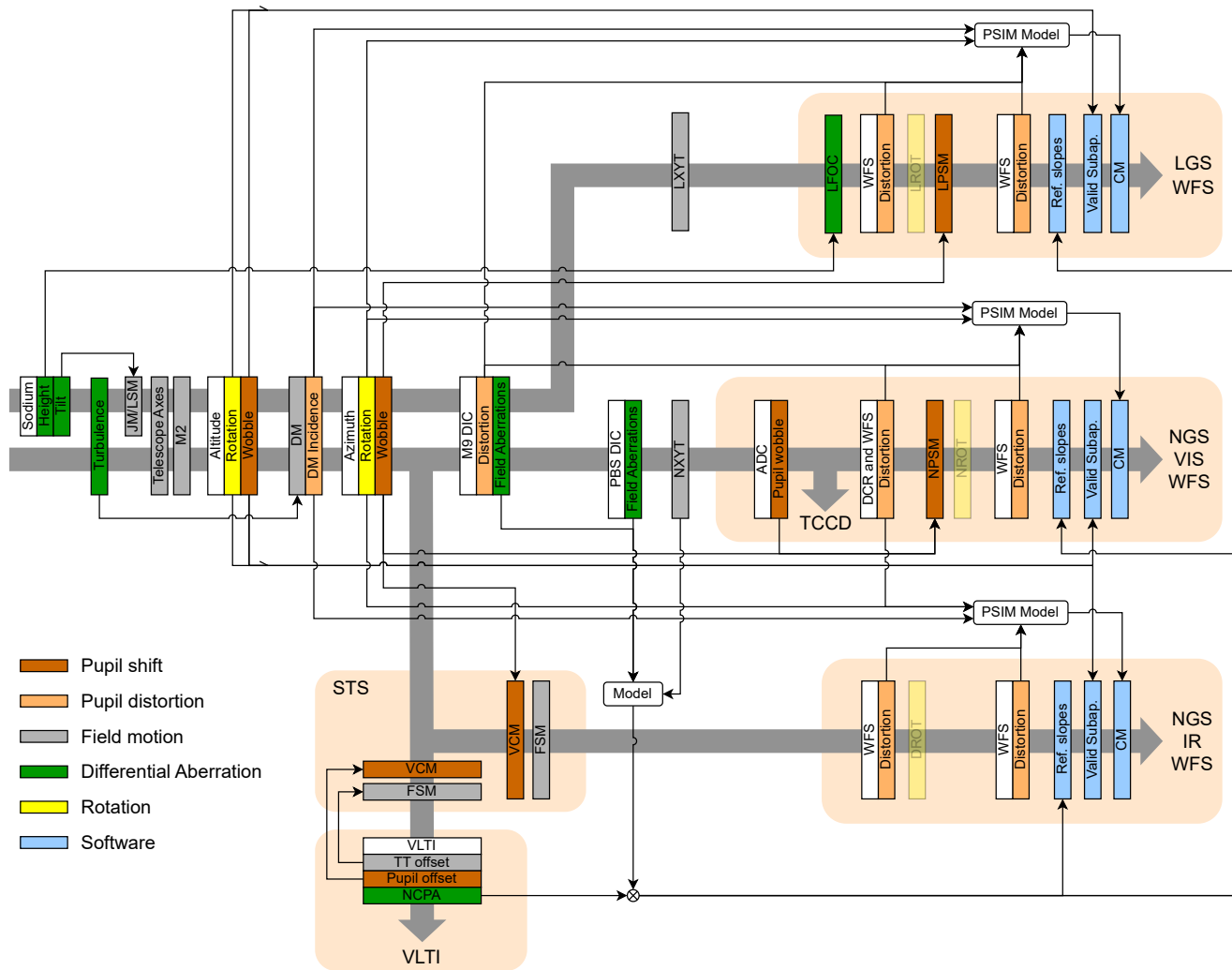


Fig. 2. Control scheme of GPAO. Disturbances and corrections are represented but sensing is not represented. The derotators LROT, NROT, and DROT are shaded to express that the hardware is physically present but that they are kept at a fixed angle.

running the framework of the VLT Software. The GPAO Instrument Workstation hosts the observation software (OS) and the instrument control software (ICS). A Detector Control Workstation (DCS) acts as command handler layer toward the camera.

The ICS controls and supervises all GPAO devices, including all devices of the former CIAO instrument. It communicates to the hardware via local controllers. It is the only interface for piloting the motion of axes. It reads the sensor telemetry and housekeeping, including those from the DM.

The OS coordinates the activities of the ICS and the RTC. It collects the states and logs of all subsystems and constructs the main state and logs of GPAO. It executes the acquisition sequence. It runs the secondary loops described in Appendix C. It prepares telemetry data to be archived. Toward the outside, it receives commands from the VLTI Supervisor, it sends commands to the Telescope Control Software, to the star separator of the VLTI and to the Multi Laser Guide Star Facility of the Unit Telescope.

3.3. Integration and testing of subsystems

Considering its importance for GRAVITY+, and the maturity of extreme-AO and LGS-assisted AO, the Gravity Plus Adaptive Optics has been implemented with a fast schedule. The design was finalized in 2022. The complete systems GPAO1 and GPAO2 were integrated and tested from the end of 2022 to early 2024, in a dedicated test bench that reproduced the telescope interfaces (Millour et al. 2024). The remaining systems GPAO3 and GPAO4 were assembled and verified at subsystems level in the different institutes. The four GPAOs were installed at the Paranal observatory in mid-2024 and regular operations of the NGS-mode started in December 2024.

3.4. Control strategy

3.4.1. Karhunen-Lo ve modal basis

The modal basis of GPAO uses approximate Karhunen-Loëve (KL) modes defined in DM command space as described in Appendix B of [Bertrou-Cantou et al. \(2022\)](#). In practice, the five first modes are enforced to be exact Zernikes (tip, tilt, focus and the two astigmatisms) and the piston is removed from the basis.

The controlled pupil is restricted to an annulus extending from 13.95% to 100% of the pupil diameter. This defines 1125 active actuators, thus 1125 independent modes, and 307 passive actuators, the latter being controlled by a linear combination of the former. The exact same modal basis is used for all wavefront sensors in all configurations (NGS_VIS, NGS_IR, LGS_VIS, LGS_IR).

The number of inverted modes (e.g. controlled modes) changes depending on the wavefront sensor in use, when building the control matrix. The values can be found in Table 1. For the high-order natural guide star wavefront sensors, the number of controlled modes is reduced when approaching the limiting magnitude. These numbers have been selected to maximize the robustness of the system while still matching the requirement in terms of Strehl ratio in the K-band under median seeing conditions. Controlling more modes will be explored in the next years, especially in the context of future J-band instruments (e.g. [Kraus et al. 2022](#); [Lacour et al. 2025](#)). When using the 40×40 WFS, the system has significant margin to control possibly up to 950 modes.

3.4.2. NGS/LGS combined control

In NGS mode, all controlled KL modes are sensed by the NGS WFS and corrected by the HRTC with the DM. In LGS mode, the tip-tilt and focus are sensed with the NGS LO WFS and the higher order KL modes are sensed with the LGS WFS. All are corrected with the DM. The filtering of controlled KL modes in each pipeline is entirely defined by the construction of its control matrix. A detailed view of the real-time dataflow is presented in Appendix D.

Because of the up/down propagation through turbulence, and because of the slowly varying distance of the Sodium layer, the tip-tilt and focus of the laser spot in the LGS WFS also needs to be controlled. The fast tip-tilt is corrected by the HRTC with the Jitter Mirror (JM) of the laser launch telescope. The JM offloads to the Laser Steering Mirror (LSM). The slow drift in focus of the laser spot is corrected by a Secondary Loop (SL) on the OS: it reads the averaged focus on the LGS WFS from the SRTC, and acts on the LFOC device accordingly.

3.4.3. Tip-tilt offload

Offloading the tip-tilt modes from the DM reduces the overall stroke budget and cancels the fitting error of the tip-tilt modes. A dynamical Gimbal mount for a DM weighing 5 kg was considered too complex for GPAO. Instead, the initial GPAO design considered offloading the tip-tilt into the M2 itself, using the available "rapid-guiding" link of the VLT (running at 100 Hz) with a small gain ensuring an offload bandwidth of a few Hertz.

When configured in rapid-guiding, the Dornier M2 of UT1-2-3 delivers tip-tilt residuals of 20 mas-rms. This is satisfactory for seeing-limited observations, but needs to be further reduced for AO-assisted systems. Unfortunately, preliminary tests during commissioning confirmed that most of the power of this noise reaches up to 100 Hz, exactly in the amplification bandwidth of GPAO (see Fig. F.1). In the meantime, the stroke of the DMs alone was found sufficient to observe up to a seeing above 1.5''. The rapid offload to M2 was therefore discarded and replaced by a slower offload to the telescope axes, every 3 s, with a gain of ≈ 0.5 . All the communication and control mechanisms remain in place, so the rapid offload could be revived if the M2 noise

is reduced in the future (an upgrade of UT3 is already planned within a few years time, UT1-2 to be defined).

3.4.4. PSIM model

The AO control scheme in GPAO is based on pseudo-synthetic interaction matrices (PSIM, [Oberti et al. 2006](#)). "Synthetic" indicates that the IMs are computed from a pure numerical model of the interaction between the DM and the WFS. "Pseudo" emphasizes that this model only depends on a small number of physical parameters that are fitted on the real system.

(I) The numerical model is based on a pure geometrical propagation of the incident wavefront: the WFS slopes are canonically given by the integrated phase differences on the lenslet sides. The DM is modeled by a set of two-dimensional (2D) influence functions defined on a high resolution Cartesian grid. Their 2D model is non-axisymmetric, and account for the inhomogeneities of the actuator gain and influence functions. This proved necessary to avoid introducing artificial fitting errors, and to properly match the desired modes.

(II) The PSIM model includes a limited number of parameters. Their numerical values can be found in Table B.1. The influence function of the DM are scaled by the DM stroke amplitude. The DM pattern is (1) stretched according to the incidence of the beam on the DM, (2) magnified by a scaling parameter to account for the magnification between the DM and the WFS, (3) rotated by an angle 'azimuth - 12.984° + a reference angle' that is calibrated on the VLT beacon, and (4) stretched by two anamorphosis (at 0° and 45°) to capture the pupil distortion. The distortions of the pupil at the Coudé focus (M9 DIC) and inside the WFS (PBS, WFS optics) can be factorized into a single, static distortion because the DROT/NROT/LROT are kept at a static position (see Fig. 2). Note that the model does not include the lateral misregistrations because these are autocorrected in hardware in operation (see Sect. 3.4.5).

3.4.5. Lateral registration between DM and WFS

The PSIM model introduced in Sect. 3.4.4 assumes that there is no lateral error between the DM and the WFS. To keep the system closed to its optimal functioning point, any alignment drift is monitored and corrected in hardware by an OS secondary loop, see Appendix C.

For the low-order wavefront sensors, this lateral alignment is obtained by centering the photometric pupil in the wavefront sensor. However, for the high-order sensors, the difference between the photometric pupil and the DM pupil is significant and thus the former cannot be used to track the lateral misregistration of the latter (see Appendix A). To do so, GPAO implements an innovative approach based on the '2D+ t ' representation of DM command telemetry ([Berdeu et al. 2024a,b](#)). In the presence of a lateral misalignment, the symmetric (cosine) part of a given spatial frequency of the command is seen with an antisymmetric (sine) small component by the WFS that leaks on the antisymmetric part of the DM command, and vice-versa. For small shifts, this coupling pattern only depends on the loop parameters (e.g., gain, latency, frequency) and is proportional to the lateral error. Contrary to other methods, this solution is noninvasive nor model-dependent ([Heritier et al. 2021](#)) while the sparsity of the signal in the '2D+ t ' Fourier domain makes it fast and with a limited bias by the wind ([Béchet et al. 2012](#); [Heritier 2019](#)).

This method has been validated on-sky during the GPAO commissioning, both with the 9×9 NGS IR WFS and with the

40 × 40 NGS HO visible WFS. Nonetheless, in strong wind conditions, it still proved to be biased by the wind in the HO VIS mode at low frequencies. As a consequence, the auto-alignment secondary loop is disabled, without noticeable loss of performances, for loop frequencies smaller than 250 Hz where only 200 modes are controlled and for which a fine alignment is not necessary.

3.4.6. Photometric pupil stability

Because the DM is actively registered onto the WFS (see Sect. 3.4.5), the photometric pupil (M2) is not necessarily centered. The mitigation implemented in GPAO is to zero the slopes measured on poorly illuminated subapertures. Practically, the median flux over the subapertures is measured during the acquisition phase, and a threshold of 15% of this value is defined in the RTC. We verified on-sky that the loop remains stable even when vignetting a large fraction of the pupil by rotating the UT dome.

This mechanism proved very effective to handle the wobbling of photometric pupil with the elevation axis, which amounted to nearly three sub-apertures (in 40 × 40 mode) when installing GPAO. Still, the drawback is that a part of the wavefront, opposite to the under-illuminated subapertures, remains uncontrolled because it falls out of the DM. Considering that an offset of 10% of the pupil diameter was unacceptable, ESO and the consortium quickly engaged into a physical realignment of the four UT telescopes. The M3 mirror was tilted to reduce the elevation wobble (see Fig. 1). The M4 mirror, closed to a focus, was adjusted to center the now stable pupil into the DM. Altogether, the photometric pupil is now always within one subaperture (in 40 × 40 mode).

3.4.7. Chopping

GPAO implements chopping based on asynchronous communications and absolute time stamping. The Interferometric Supervisor Software (ISS) receives the chopping parameters (amplitude and direction on sky, period, duty cycle and start time of a few seconds in the future) from the scientific instrument. The ISS forward these parameters to the M2 controller and to the GPAO OS. The GPAO OS forwards these parameters to the HRTC. Once the start time is reached, the HRTC determines the current state (“on-sky” or “on-science”) of the current frame purely based on the period and the absolute time. There is no other synchronization between the M2 and the HRTC rather than sharing the same time server. The HRTC freezes the loop during the “on-sky” phases, and resumes the loop during the “on-science” phases. Freezing in the RTC means that the last command is kept unmodified, without feedback from the measurements, nor accumulation of leaks or anti-windup. The SRTC monitors and recorders ignore the “on-sky” phases when relevant (e.g., to compute the offloads).

3.4.8. Non-common path aberration

As discussed above, non-common path aberrations (NCPA) inside the WFS and inside the VLTI can be factorized into a single, static aberration because the DROT/NROT/LROT are kept at a static position (see Fig. 2). These NCPA are measured all the way to the IRIS guiding camera of VLTI (Gitton et al. 2004; Pourré 2024), using the telescope Nasmyth beacon in day time. Sequentially on each controlled mode starting with defocus, a

modulation is injected into the closed AO loop at the level of the WFS slope measurements. The variance of the IRIS image, a proxy of the Strehl ratio, is computed for each recorded frame. The modulation on each mode contains a high 25 Hz frequency and two periods of a low 0.25 Hz frequency. The amplitude of the 25 Hz detected on IRIS reaches a minimum when the slow period crosses the NCPA offset (the Strehl maximum). Two periods are recorded, giving at least three consecutive minima and their temporal spacing is a robust estimate of the NCPA offset.

Theoretically, the previous calibration is no longer valid when the beam crosses the M9 and PBS dichroic at a different location, that is when the NGS WFS is off-axis. This field-dependent NCPA is modeled by a low-order polynomial dependence of the astigmatisms modes. The model can be calibrated on measurements made on the beacon at various off-axis positions, thanks to the steering capability of the QSM. As of today, this calibration is set to zero since no significant field-dependent NCPA has been observed in VLTI.

4. Operations and performances

4.1. Operations

4.1.1. Operational modes

GPAO supports the four modes described in Table 1 (NGS_VIS, NGS_IR, LGS_VIS, LGS_IR), consisting of various combination of the wavefront sensors. Seeing-limited mode (no AO correction) and seeing-enhancer mode (only LGS correction) are virtually useless for the spatially filtered instruments of VLTI, and are thus not supported.

4.1.2. Automated acquisition

A VLTI preset (change of target) is triggered by the scientific instrument, namely PIONIER (Le Bouquin et al. 2011), GRAVITY (GRAVITY Collaboration et al. 2017), or MATISSE (Lopez et al. 2022). The preset is sent to the VLTI Supervisor, which forwards it to the various subsystems of the VLTI: telescope, delay lines, STS, laboratory configuration, and GPAO. GPAO immediately initiates its (re)configuration and setup, in parallel to the telescope slewing. Relevant to GPAO, the preset contains the desired AO mode (see Sect. 4.1.1), the magnitude of the natural AO guide star, the coordinates of the AO guide star, the desired coordinate for the LGS guide star, and the on-axis coordinates of the telescope. The difference between these coordinates drives the position of the NXYT, the LXYT and of the Field Steering Mirror (FSM), and therefore the off-axis offset of the wavefront sensors at the Coudé focus. The NGS wavefront sensor is setup to a low amplification, and to a rate adapted to detect the given magnitude without risking a sensor over-illumination. A filter is possibly inserted to reduce the flux on very bright objects. If requested, the LGS wavefront sensor is setup at a fixed frame rate of 1000 Hz and an amplification gain of 400. The LGS system is also configured and the laser is propagated as soon as the telescope has reached the coordinate and follows a blind trajectory. The LSM of the Laser Launch Telescope is setup from a elevation-based pointing model, to compensate for the flexures, so that the laser spot immediately appears within the field-of-view of the LGS WFS. The LFOC device is setup to the expected distance of the Sodium layer at the time of the preset.

The acquisition with GPAO, fully automated by default, is composed of three steps: detecting the star (DETCGS), optimization of camera and loop parameters (OPTCGS), and closing

the loop (STRTCAG). In LGS modes, these three steps are first applied to the laser guide star, and only then to the natural guide star. The DETCGS executes a raster with the QSM (for the NGS) or with the JM (for the LGS) and moves the telescope (for the NGS) or the LSM (for the LGS) to the position of maximum of flux. Then, the OPTCGS raises the amplification gain up to the maximum permissible value (42 in IR WFS or 1000 in LGS and VIS WFSs) and estimates the actual magnitude of the star. For the NGS VIS WFS only, this magnitude serves for an optimization of the camera amplification gain and frame rate. Apart from this specific point, the acquisition is strictly the same whether the natural guide wavefront sensor is IR or VIS. The DM/WFS registration is then optimized following the strategy presented in [Berdeu et al. \(2024a\)](#). It consists of modulating a subset of KL modes on the DM, and fitting the measured interaction matrix with a fast correlation method. The last step of the optimization estimates the median flux per subaperture, and updates the threshold of the RTC below which the gradients are considered invalid and forced to zero. At this point, the STRTCAG is executed and all loops related to this WFS are closed, including offloads and secondary loops. Once all required wavefront sensor(s) are acquired, GPAO raises to state “Coudé Guiding”, which informs the scientific instrument to pursue its own acquisition.

The automatic acquisition works well when there are no other bright targets within a few arcseconds around the guide star. For more complex fields, the operator has the possibility to manually execute the acquisition steps one by one to specifically select the correct guide star.

4.1.3. Coordination with science observations

A typical observation block at the VLTI lasts for one hour and includes several individual exposures, with a typical overhead of a few seconds between exposures. The GPAO OS is informed of the beginning and end of every exposure.

Telemetry GPAO records 30 s of AO telemetry at the start of each science exposure. This telemetry includes all frames for the “loop data” (slopes, intensities, commands, chopping state) and a sub-sampling at 10 Hz for the “pixel data” (pixel stream). The files are stored on the observatory servers for one month, for technical use, but the ESO central archive system does not allow them to be made externally available. At the end of each exposure, the OS collects and forwards the necessary information to build the AO-related part of FITS header.

Passive Support The Unit Telescopes incorporate a mechanism (M1PMOVE) to regularly re-center laterally the M1 mirror itself inside its cell. This is especially important when observing at low elevation. When triggered, the lateral motion of M1 creates a strong tip-tilt and a large step of optical path delay, which can make the fringe-tracker lose the tracking for several seconds. Therefore, the automatic, regular M1PMOVE mechanism is deactivated when the UTs are used for VLTI. Instead, GPAO requests the M1PMOVE only at preset.

4.1.4. Maintenance and monitoring

All calibrations are executed in day-time. The calibration unit allows recalibrations to be performed of the internal alignment, pixel scale, reference slopes, and conversion gain and amplifica-

tion gain of the camera, for the NGS VIS and the LGS wavefront sensors. No such tool exists for the NGS IR wavefront sensor. The dark level of all cameras are re-calibrated by closing the corresponding shutters. The PSIM parameters (see Sect. 3.4.4) can be re-calibrated by measuring interaction matrices using the Nasmyth beacon. The DM reference vector used to flatten the DM in open-loop can be re-calibrated using the Nasmyth beacon. The template inverts a zonal interaction matrix keeping 1100 eigenvectors to create a zonal control matrix, then closes the loop for a few seconds without any modal or zonal leaks, and records the DM position.

The daily health check includes a measurement of the gain of all actuators of the DM, to verify their functionality. The mean gain is trended over time as well as the number of nonfunctioning actuators inside the clear aperture (currently only one known in GPAO2). The daily health check also includes a measurement of the DM flat reference vector. It is used for trending only and the actual vector installed in the system is not updated automatically.

4.2. Verifications

4.2.1. Transmission

Figure E.1 in Appendix E shows the measured flux as a function of source magnitude. From this the following zero points can be derived for GPAO 1 to 4 for a zero magnitude star in the Gaia G_{RP} band: 1.12, 1.32, 1.32, 1.01×10^{11} e/s. The ratio between the best and the worst GPAO is 0.75. For the 40×40 WFS running at 100 Hz, the available flux is ≈ 5 electrons per frame and per subaperture for a magnitude 13. This level of illumination corresponds to the operational limiting magnitude in NGS_VIS mode. The zero-point of Gaia G_{RP} (24.7619, see [Riello et al. 2021](#)) corresponds to 5.45×10^{11} e/s when scaled to the collecting area of the Unit Telescopes (49.26 m^2) with respect to that of Gaia (0.723 m^2). The chromatic shape of GPAO matches well the one of the Gaia G_{RP} band-pass. The absolute peak transmission of Gaia G_{RP} being 74%, the absolute peak transmission of the visible wavefront sensors of GPAO is in the range of 13.7% to 17.9% (end-to-end, all included).

In the infrared, a fit of Fig. E.2 gives the following zero points for GPAO 1 to 4 for a zero magnitude star in the K-band: 1.62, 2.06, 1.51, 1.42×10^{10} e/s. When running at 100 Hz, the illumination of five electrons per frame and per subaperture is reached at a magnitude 11, which again corresponds to the operational limiting magnitude of the NGS_IR mode.

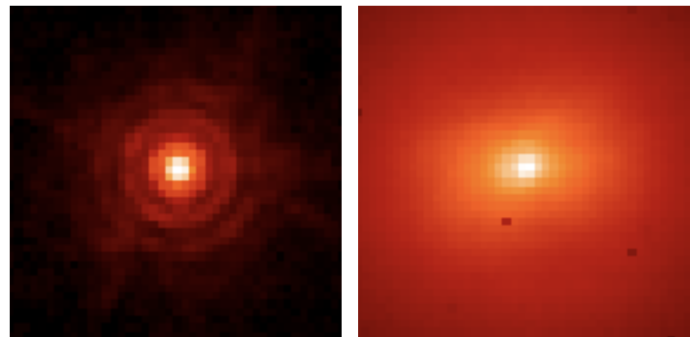


Fig. 3. Images of unresolved stars (point spread function) measured in K-band with the IRIS guiding camera of VLTI, corrected by GPAO in NGS_VIS in the bright regime (left, $G_{RP} = 5$, Strehl 77%) and faint regime (right, $G_{RP} = 12$, Strehl 11%). The flux is represented in log scale.

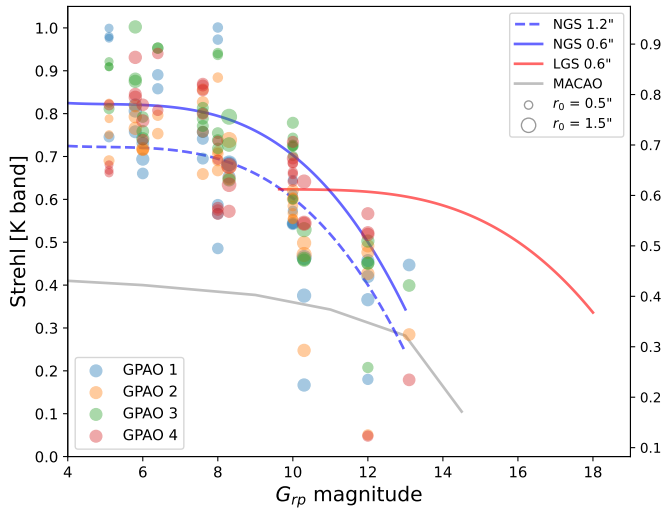


Fig. 4. Strehl in the K-band versus the Gaia G_{RP} magnitude of the guide star. Points indicate the measurements with GPAO in NGS_VIS mode. The seeing conditions are proportional to the diameter of the point. The blue curves are the expectations for GPAO in NGS_VIS mode and two seeing values, the red curve is the expectation for GPAO in LGS_VIS mode with seeing 0.6''. The gray curve shows the performance of the former MACAO system of VLTI.

4.2.2. Transfer function

Measurements and model of the transfer function is described in Appendix F. It includes the delay introduced by the integration time, the hold, and the mechanical response of the DM. It also includes an additional pure-delay term T_d to account for the transferring, buffering and computations of data. We adjust this model to the measured rejection functions. Representative results are shown in Fig. F.1. The rejection bandwidth at -3 dB is at 45 Hz in the visible and 50 Hz in the infrared, while MACAO reached only 18 Hz (Arsenault et al. 2004). The rejection bandwidth is now comparable to those of SPHERE or other extreme AO.

The fitted integration gain K_i are slightly smaller than the value actually used in the controller (0.5). There are several possible explanations such as optical gains or overestimated DM mechanical gains in our geometrical model. The slightly larger actual integration gain in the infrared sensor explains the higher rejection bandwidth. In theory the integration gains could be tuned closer to the stability limit to further improve the rejection. This was discarded, however, because the optical gain can vary with the seeing conditions.

In the visible wavefront sensor, the expected pure-delay $T_d \approx 830 \mu\text{s}$ is the sum of the readout time of the OCAM2 (500 μs , equal to the maximum frame rate), the time to extract the pixel from the camera (47 μs , from manufacturer), the buffering in the frame-grabber (110 μs , frame sent in 5 packets) the HRTC latency (80 μs , measured at the oscilloscope), the time to transfer the command to the DM at 1 GbE (21 μs), and the buffering inside the DM electronic (70 μs , from manufacturer). This prediction matches adequately the measured pure-delay of $T_d = 856 \mu\text{s}$, therefore validating our understanding of the dynamic of the system. A total loop delay is often computed by adding the pure-delay (above), half the DM rise time (400 μs), and 1 full frame to account for the digitalized controller. This total loop delay is 2.4 frames at 1 kHz frame rate.

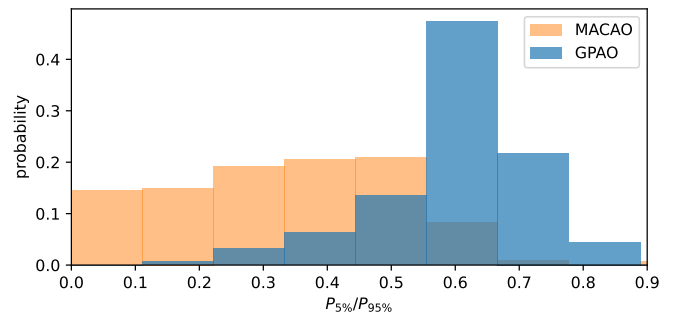


Fig. 5. Comparison between MACAO (entire year 2023) and GPAO NGS_VIS (from December 2024 to May 2025) of the $P_{5\%}/P_{95\%}$ injection metric histograms for the GRAVITY fringe tracker. The flux dropouts, represented by $P_{5\%}/P_{95\%}$ values close to zero, are significantly reduced by GPAO.

The NGS IR detector uses a reset and double-correlated read sequencer. It reduces the duty cycle, but also reduces the pure-delay with respect to our basic model of Appendix F. There is no buffering in a frame grabber. Finally, the computation time is shorter because there are fewer pixels and slopes to process. Altogether, it explains why the measured pure-delay ($T_d = 515 \mu\text{s}$) is shorter than in the visible wavefront sensor.

4.2.3. Piston control

Following the method presented in Woillez et al. (2019), a piston conversion factor for the first controlled modes is measured by injecting a modulation on the DM and detecting it with the GRAVITY fringe tracker. The conversion factor is the ratio between the piston measured in $\mu\text{m-rms}$ and the modal modulation in $\mu\text{m-rms}$. The modal basis of GPAO is defined to be piston-free when integrating the wavefront with a uniform weight over the

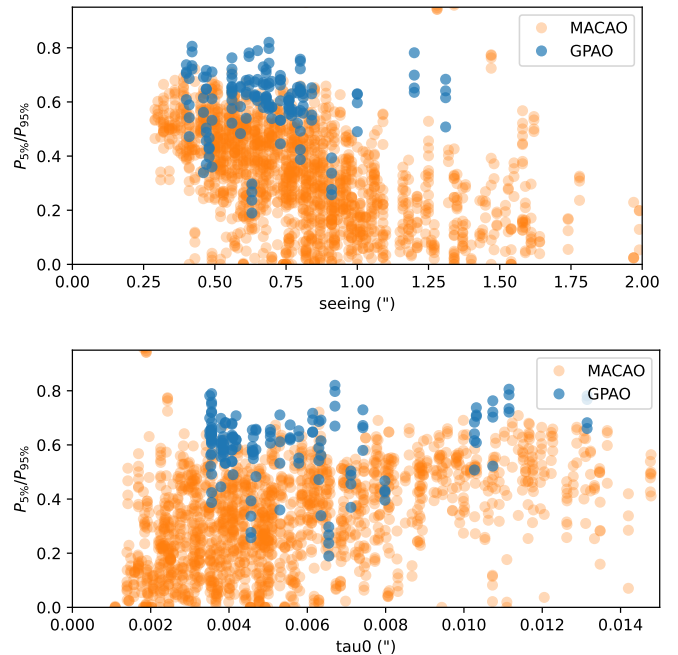


Fig. 6. Comparison between MACAO and GPAO of the $P_{5\%}/P_{95\%}$ injection metric histograms for the GRAVITY fringe tracker versus the atmospheric conditions.

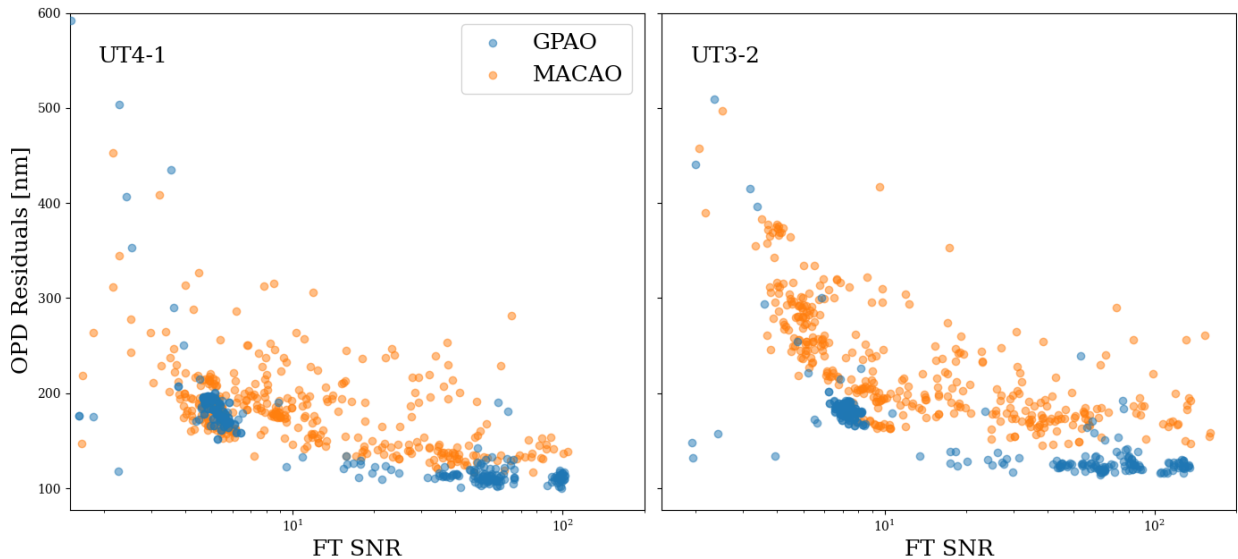


Fig. 7. Comparison between MACAO and GPAO of the optical path difference residual after fringe tracking, as a function of the signal to noise ratio in the GRAVITY Fringe Tracker. Data are shown for two independent baselines, which are representative of the performance of the entire array.

telescope pupil. When accounting for the single-mode apodisation of the pupil by the GRAVITY fiber, the model predicts significant conversion factors for focus and the second spherically symmetric mode (and all modes with radial-only dependency). We measure a conversion factor of 0.57 for the focus (0.35 expected) and 0.07 for the first spherical (0.05 expected).

4.2.4. Acquisition time budget

The duration of the GPAO acquisition is measured from the moment the telescope delivers the beam (first cycle of telescope active optics), to the moment the GPAO adaptive optics loop is closed. Therefore, all setup activities that are parallelized with the telescope slew are not accounted for. The acquisition in NGS mode have a median duration of 110 seconds, with 95% of the acquisitions lasting fewer than 180 seconds. The LGS acquisitions are typically 30 seconds longer than the NGS.

Changing GPAO mode requires some hardware (closing/opening shutters, moving HO/LO stage, turning filter wheels) to be reconfigured, but also the full shut down and restart of all the individual SRTC and HRTC processes. This action takes about 200 seconds.

4.3. System-level performances

4.3.1. Strehl versus magnitude and seeing

The point spread function (PSF) of the system is commonly estimated by observing unresolved stars. Typical images of PSF observed with the IRIS guiding camera of VLTI are shown in Fig. 3. The system was setup with the default NCPA, calibrated on the Nasmyth beacon with the method detailed in Sect. 3.4.8. In the bright regime, the PSF is dominated by the diffraction pattern of the Unit Telescope aperture and spiders. In the faint regime, the PSF is dominated by the residual of uncorrected turbulence. The elongated aspect of the halo indicates the direction of the wind because the system is dominated by the temporal error. Most of the time, the PSF is dominated either by the diffraction of the aperture or by the residuals of the fast atmo-

spheric turbulence, as presented here. Occasionally, the PSF is dominated by the so called “low wind effect” as also seen in others high contrast instruments (see for instance Milli et al. 2018). Preliminary analysis indicates that the effect is more pronounced in telescopes UT1-2, which matches the fact that the spiders of UT3-4 have been re-coated with special painting to increase their thermal coupling with surrounding air. Re-coating the spiders of UT1-2 will be implemented in the next year as part of the GRAVITY+ project.

Figure 4 presents the measurements of Strehl collected during the commissioning nights versus seeing and magnitude of the guide star for the NGS_VIS mode. Important to notice, the system was still under test and optimization at the time. Especially, the NCPA were not always properly calibrated. Nevertheless, the values closely match the predictions. The peak performances are significantly improved with respect to the former MACAO that was reaching a top Strehl of 0.4 on the brightest targets in the best atmospheric conditions. The limiting magnitude of GPAO is about the same as MACAO. This is expected since the faint-end will be covered by the LGS mode once available.

Table 2. Performances of the four modes of GPAO and of the former MACAO and CIAO systems.

AO	Strehl ^a K-band	Bright [mag]	Faint ^b [mag]	Filter
MACAO	40 %	9	13	V
NGS_VIS	75 %	8	12	G_{RP}
LGS_VIS ^c	60 %	13	17	G_{RP}
CIAO	40 %	9	12	K
NGS_IR	40 %	9	12	K
LGS_IR ^c	60 %	9	12	K

Notes. ^(a) Strehl obtained under nominal weather conditions on a bright target. ^(b) Operational limit with reduced performances. ^(c) The performances of the LGS modes are preliminary and have been only roughly verified on sky .

4.3.2. Injection stability

Interferometric fringe tracking is particularly sensitive to occasional flux dropouts, which can make the fringe tracker lose the white-light position and lead to a long recovery time before a truly coherent integration can resume. Tatulli et al. (2010) theorized the effect of improved AO in the coupling into a single mode fiber, with a specific emphasis on the stability of the coupling for optical interferometry. We quantified the improvement brought by GPAO by using the same metric as used for NAOMI in Woillez et al. (2019). This metric, noted $P_{5\%}/P_{95\%}$, represents the ratio of the flux at low 5% injection to the flux at high 95% injection. It tends to one for a perfectly stable injection, and tends toward zero in the presence of regular flux dropouts. Figure 5 compares the histogram of the $P_{5\%}/P_{95\%}$ metric for GPAO (blue) and MACAO (orange) for each of the UTs. The measurements are from the GRAVITY Fringe Tracking instrument, in the K-band. The clear shift toward higher $P_{5\%}/P_{95\%}$, with a median of 0.31 for MACAO and 0.62 for GPAO, demonstrates a tremendous improvement in the stability of the flux injected into the single mode fiber of the fringe tracker.

A decisive advantage of GPAO is its improved robustness against degraded atmospheric conditions, illustrated in Fig. 6. The former MACAO system was saturating for seeing larger than 1'', with devastating effects on the Strehl because of the extended influence functions of the curvature deformable mirror. Thanks to the improved stroke, and the use of a mirror technology with localized influence functions, GPAO safely operates even with seeing larger than 1.5''. GPAO can also operate in faster coherence time thanks to a maximum frame rate of 1000 Hz with respect to 500 Hz for MACAO. When comparing the statistic of turbulence at Paranal, it corresponds to an increase in operational time for VLTI by 30% (now reaching nearly all conditions).

4.3.3. Fringe tracking performances

Figure 7 compares the optical path delay residuals as a function of the S/N of the Fringe Tracker for GPAO NGS_VIS and MACAO, for two independent baselines. The faint end displays the expected dependency between the S/N and the performance for a noise-limited system. The bright end shows the expected plateau of a rejection-limited system. The improvement brought by GPAO is obvious, with residuals just above 100 nm compared to 150 nm when the fringe tracker was fed by MACAO. The much smaller scatter is synonymous of more reliable operation.

This positive outcome of the installation of GPAO was not anticipated. The best explanation comes from the change in deformable mirror technology. The MACAO curvature deformable mirror, with influence functions highly coupled to the piston mode, was replaced by the ALPAO deformable mirror with localized influence functions. We believe that the MACAO system was somehow coupling the high spatial and temporal frequency atmospheric perturbations back into a high temporal frequency piston.

4.4. Discussion on bright and faint end

Table 2 gives a condensed overview of the GPAO performances. On the one hand, the GPAO system in GPAO_VIS mode outperforms the former MACAO system on bright stars by a factor larger than two. This is expected because MACAO was designed as a general purpose facility while GPAO in NGS_VIS mode is optimized for the peak performance in the bright regime.

On the other end, the faint end of GPAO NGS_VIS is similar to MACAO, when considering the mean Strehl only (see Sect. 4.3.1). However, combined with the improvement in Strehl stability (see Sect. 4.3.2) and the improvements in OPD residuals (see Sect. 4.3.3), the interferometric performances of the VLTI with GPAO in NGS_VIS mode are significantly increased with respect to MACAO, even in the faint end. This is demonstrated by several observations both for the bright end and the faint end as presented in the next section, that were impossible with MACAO.

The limiting magnitude of GPAO in NGS mode is close to its fundamental limit of $G_{RP} \approx 13.1$ (see Appendix G). At first order, the difference matches the transmission detailed in Sec. 4.2.1. The limiting magnitude of the LGS mode is significantly further away from its fundamental limit of $G_{RP} \approx 20.3$. It comes from the choice of using 4×4 subapertures in the low-order sensor instead of the full telescope aperture.

5. Enabling new science

This section presents the new science enabled by GPAO coupled to on-sky interferometric observations. We illustrate this new range of capabilities with several archetypical objects that were acquired during the end-2024 commissioning.

5.1. High-redshift quasar $z=4$

Extragalactic science depends critically on sensitivity. The implementation of G-Wide (GRAVITY+ Collaboration et al. 2022), see Sect. 2.3) enabled the first dynamical mass measurement of a $z \sim 2$ Super Massive Black Hole (SMBH) (Abuter et al. 2024). To push even further into the early Universe and to build statistical samples probing SMBH-galaxy coevolution across cosmic time requires an increase in both sensitivity and sky coverage for GRAVITY, because of the need for off-axis reference stars to perform AO correction and fringe tracking. As discussed in Sect. 4.3, the new GPAO systems with high-order corrections achieve both through the improved Strehl and fiber injection efficiency that increases the S/N on the interferometric observables and pushes the fringe tracking limiting magnitude to fainter objects.

Expanding the capabilities of GRAVITY to dynamically measure black-hole masses at earlier times and fainter objects is also very timely given recent results from the James Webb Space Telescope (JWST). JWST-discovered broad-line AGNs at $z > 4$ suggest a fast growth of black holes that outpaces the growth of their host galaxy and leads to over-massive black holes (e.g. Maiolino et al. 2024). These masses are derived from local scaling relations extrapolated to high redshift and indeed significant changes in the gas structure can lead to up to two orders of magnitude difference in the inferred mass (e.g. Maiolino et al. 2025; Naidu et al. 2025). Direct measurements of SMBH masses are therefore critical in our understanding of black-hole growth.

Here, we illustrate the observations of a $z \sim 4$ quasar with GPAO-NGS in combination with the G-Wide mode. We selected SMSS J052915.80-435152.0 ($m_K = 13.9$), hereafter called J0529-4351, which was discovered to be “the most luminous quasar in the Universe” (Wolf et al. 2024). Its high luminosity would predict a very large BLR differential phase signal and its redshift places both the H β and H γ recombination lines in the K-band. J0529-4351 is also located 22 arcsec away from a star with $G_{RP} = 12.1$ and $m_K = 11.0$ (see Fig. 8 left), making it a good test of the capabilities of GPAO-NGS at the faint end as well as the new FT limiting magnitude.

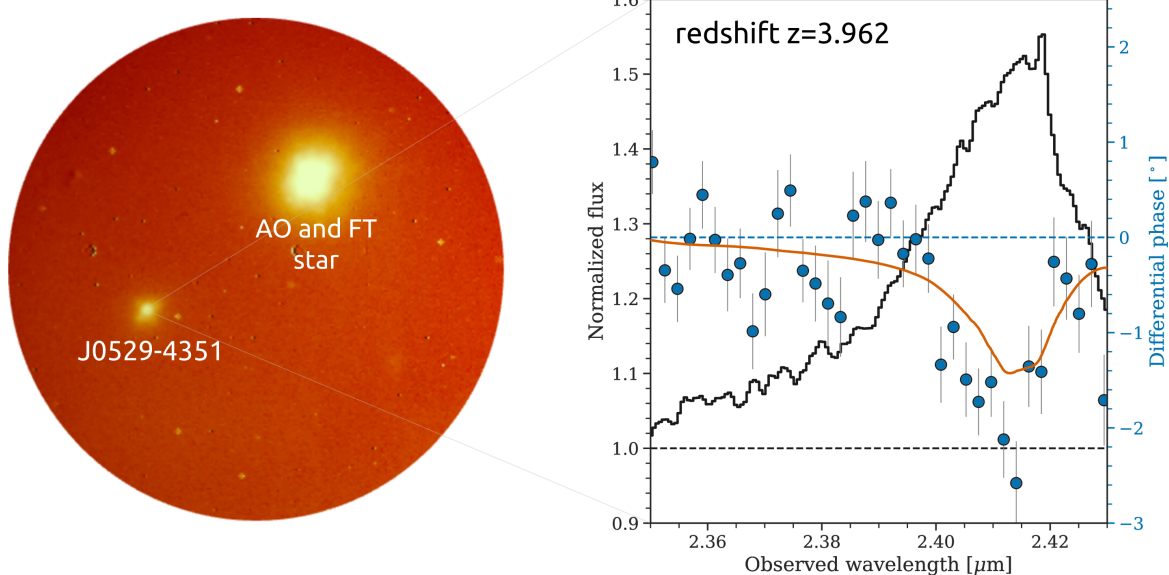


Fig. 8. Left: GRAVITY H band Acquisition Camera image of the observation of J0529-4351 showing the quasar and AO/FT reference star. On sky the separation is $22''$ but the VLTI optics bring them to GRAVITY in separate beams with a separation of about $2''$ **Right:** Averaged differential phase spectrum of J0529-4351 (blue points) across the H β emission line (black line). An initial BLR model fit to the line profile and differential phase (red line) shows a much smaller BLR and SMBH mass.

We observed J0529-4351 with the MEDIUM spectral resolution grism and COMBINED polarization mode over five nights. The atmospheric conditions ranged from $0.4''$ to $1.1''$, and required overall good atmosphere conditions given the large separation between the AO/FT star and the quasar, which affects the anisopistonic errors. The total usable data is about 7.8 h on-target, for which the improved performance of the AO for seeing $\geq 0.5''$ is crucial, and previously not possible with MACAO. The raw data with DIT=100 s and NDIT=4 were reduced through the GRAVITY pipeline to produce complex visibilities and differential phases. The differential phase data were analyzed following the methodology described in Abuter et al. (2024). In the right panel of Fig. 8, we show the total photometric flux of J0529-4351 across the H β emission line as well as the average differential phase spectrum by combining the longest three baselines (UT1-UT4, UT1-UT3, and UT2-UT4). The redshift of the quasar places the line near the edge of the wavelength range of GRAVITY and therefore cuts off part of the red wing. Nevertheless, we strongly detect the H β line that peaks at $2.41\text{ }\mu\text{m}$ and has a FWHM of $\sim 3200\text{ km s}^{-1}$ with an underlying blue wing offset by $\sim 2000\text{ km s}^{-1}$ and a FWHM of $\sim 7000\text{ km s}^{-1}$. We measure a typical noise of $\sim 1^\circ - 2^\circ$ per spectral channel and per baseline within the H β line for the total observing time. The observations show a strong dip in differential phase, which demonstrates that we spatially resolve the BLR in J0529-4351. However, the differential phase signal does not follow a canonical “S-shape”, which indicates a motion departing from pure-Keplerian motion. This is a potential signature of significant radial motion in J0529-4351, which has also been reported in GRAVITY observations of local AGNs GRAVITY Collaboration et al. (2024a), but which has never been observed at high-redshift. The modeling of the BLR in this complex environment would indicate a BLR size and SMBH mass a factor of two smaller than the size predicted from scaling relations, with a measured size from GRAVITY of 1.2 pc , and a SMBH mass of $10^{9.6}\text{ M}_\odot$. We caution the reader these are only preliminary results and a full analysis of the GRAVITY data

for this quasar, including the H γ line, is beyond the scope of this paper and will be presented in an upcoming dedicated paper.

5.2. Extragalactic stellar interferometry

Stellar physics has been a dominant field of optical/infrared interferometry (or “stellar interferometry”). With the capability to observe faint targets and wide off-axis fringe-tracking targets, it becomes possible to extend stellar interferometry outside of the Milky Way in our local Universe. We demonstrate this capability on the Large Magellanic Cloud (LMC), which was observed on 27 September 2024 using GPAO and G-Wide. We focused on the dense central star cluster R136 of the Tarantula Nebula that hosts a large concentration of O and Wolf-Rayet stars within a 5 parsec region (Feast et al. 1960), and are the most massive stars known currently in the Universe (Crowther et al. 2010). These observations allowed the acquisition of targets in crowded fields to be validated, using the WFS technical camera for the acquisition of the AO star (see 3.2.2), and the GRAVITY Acquisition Camera in G-Wide mode (GRAVITY+ Collaboration et al. 2022), see Fig. 9, upper panel. We observed the star R136c (BAT99 112) with a magnitude $m_K = 11.31$, using the star R136a1 at a separation of $3.35''$ for AO ($m_V = 12.8$) and FT ($m_K = 11.15$). The observations were performed in good weather conditions, with seeing $\sim 0.45''$ and wind speed $\sim 7\text{ m s}^{-1}$. In only 8 min of exposure on source (DIT=3 s) and a spectral resolution $R \simeq 20$, the precision obtained on the closure phases is of the order of $\sim 1\text{ deg per channel}$ (see Fig. 9, lower panel). We analyzed the closure phases to look for a signature of binarity. Despite the short observing time on target, we can rule out binary companions in R136c with a flux ratio of ≥ 0.1 and separation $\gtrsim 5\text{ mas}$. These observations exclude massive companions ($M \gtrsim 20\text{ M}_\odot$) at large separation $\gtrsim 250\text{ au}$. Significantly stronger constraints on the flux ratio and the separation 100–1000 au can be obtained in the future with longer integration and improved uv-coverage. These constraints are very complementary to RV data, which are

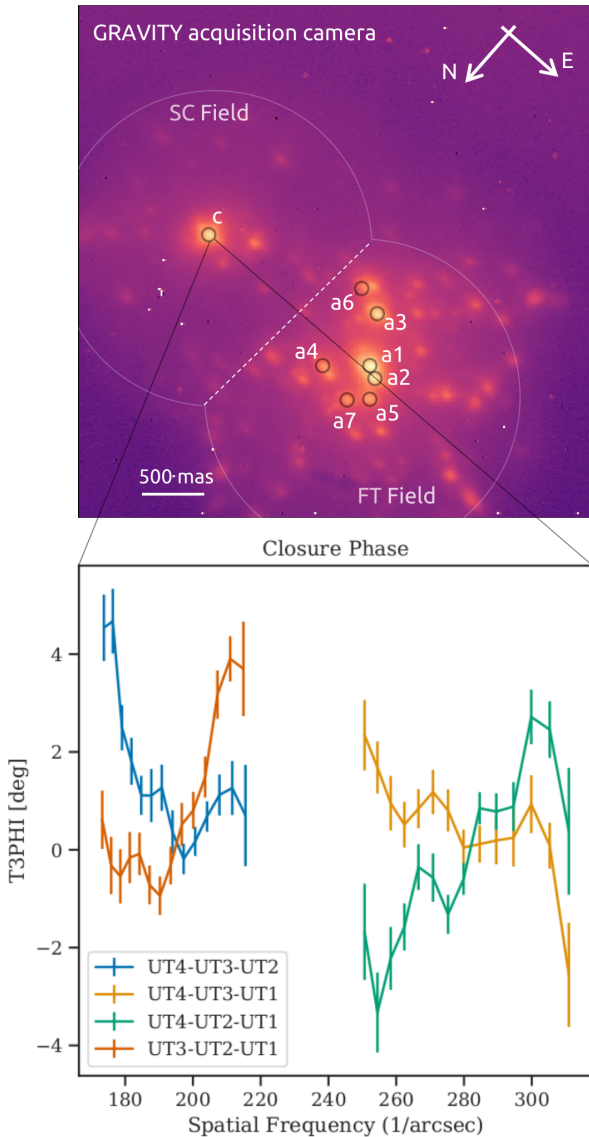


Fig. 9. **Upper panel:** RMC 136 seen on GRAVITY Acquisition Camera. **Lower panel:** Closure-Phases of RMC 136c observed with G-Wide and GPAO. These observations are close to the limiting magnitude in NGS_VIS mode and will greatly benefit from the LGS next year.

mainly probing periods shorter than tens of years, corresponding to companions with a separation $\lesssim 100$ au.

5.3. High-resolution spectroscopy of exoplanets

The upgrade from MACAO to the high-order correction of GPAO is crucial for the observations of exoplanets. This science case benefits both from the improved rejection of the starlight and the better flux injection of the planet in the science fiber. Figure 10 showcases the reduction in the glow around the bright star HR 8799. The brightness of the halo is reduced by a factor 9.1, 2.8 and 2.0 at the separation of the planets e (400 mas), d (690 mas) and c (955 mas) respectively. In the following, we illustrate the resulting improvement of scientific capabilities with high-resolution spectroscopy of exoplanets and brown dwarfs.

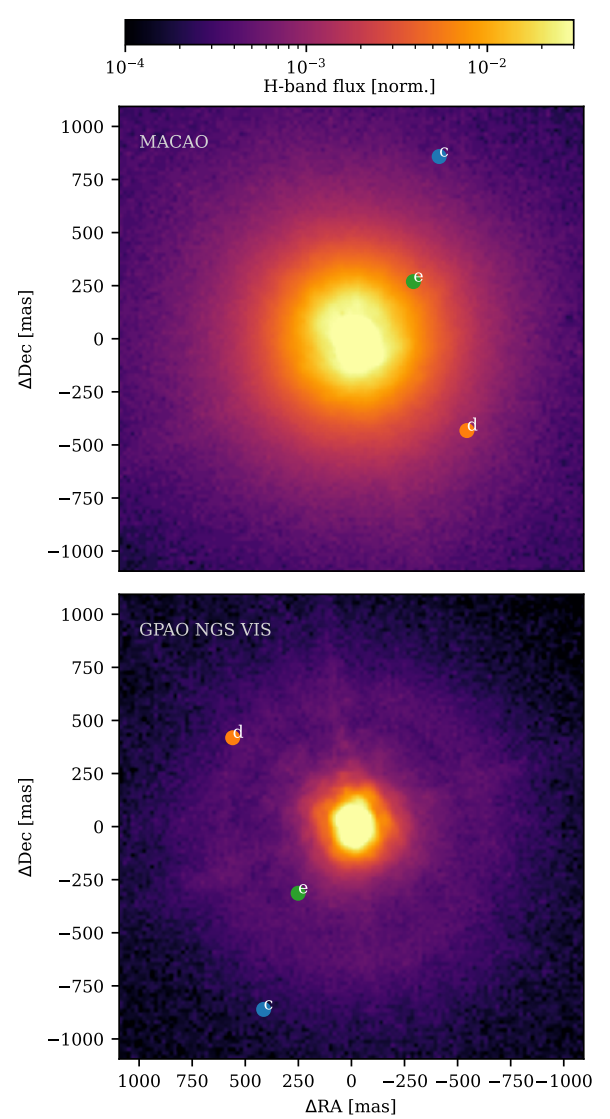


Fig. 10. Image of the GRAVITY Acquisition Camera (H-band) showing the saturated PSF around HR 8799, when observed with MACAO (top) and with GPAO in NGS_VIS (bottom). The scale is normalized to the maximum of the image. The ring structure corresponds to the spatial cutoff frequency of GPAO when controlling 500 modes. The positions of the known exoplanets are shown for reference.

5.3.1. High-resolution spectroscopy of HR 8799 e

The young giant planet HR 8799 e was the first exoplanet detected using optical interferometry (GRAVITY Collaboration et al. 2019b). This object is located at a separation $\sim 0.4''$ from its host star and has a magnitude of 15.9 mag in the K band. HR 8799 e was re-observed with GRAVITY dual-field using GPAO instead of MACAO during the night of 28 September 2024, with a seeing $\sim 0.7''$. The observing time on target was only 0.3 h, but shows the significant improvement in terms of sensitivity compared to previous observations. The new spectrum obtained with GPAO is shown in Fig. 11, together with an old HR 8799 e spectrum from 28 August 2021 obtained with MACAO in 0.4 h on HR 8799 e, both with a spectral resolution $R \sim 500$. For a comparable exposure time on target, an improvement in the S/N of a factor of ~ 10 can be clearly seen. This improvement is both consistent with an improvement of flux in-

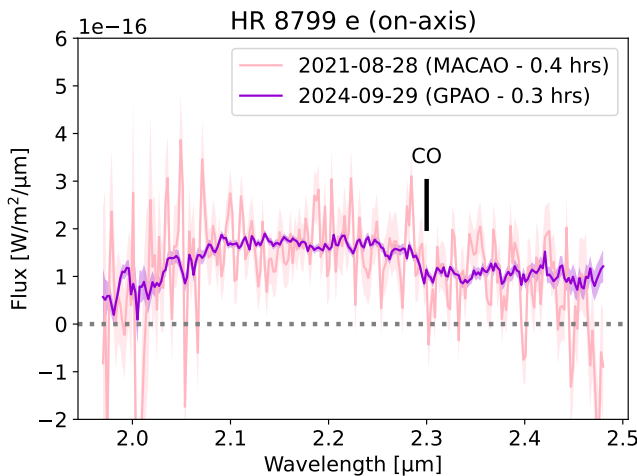


Fig. 11. GRAVITY on-axis spectrum of the young giant planet HR 8799 e obtained with the new GPAO system and with the old MACAO system.

jection in the SC fiber by a factor ~ 3.5 and the reduction of noise by a factor ~ 2.5 . The improvement of flux injection is consistent with the increase in the Strehl ratio for a $G_{RP} = 5.4$ star from GPAO to MACAO, as shown in Fig. 4. The noise reduction originates from a better rejection of stellar photons and longer integration (DIT=100 s compared to DIT=30 s in 2021), the latter being due to improved fringe-tracking and reduced vibrations, as shown in Section 4.3.3. In only 0.3 h, it is possible to clearly identify the CO ro-vibrational lines at $2.3\text{ }\mu\text{m}$ in the spectrum of HR 8799 e. With long exposure, this new capability opens up the possibility of high signal-to-noise ratio spectroscopy in order to measure accurate C/O elemental abundances or time-resolved spectroscopy for young exoplanets, such as HR 8799 e or β Pic b.

5.3.2. Spectroscopy down to $m_K \sim 21$

We observed the ultra-cool brown dwarf HD 4113 C (Cheetham et al. 2018) with GRAVITY and GPAO during the November 2024 commissioning run, together with the FAINT mode on GRAVITY (Widmann et al. 2022). This substellar companion is located at a separation of $0.7''$ from its host star, with a magnitude about 21.0 mag in the K band (Vega magnitude), significantly fainter than the faintest companion successfully observed with the old MACAO system, which was 51 Eri b at about 18.5 mag in the K band at a similar separation. The observations were obtained in average weather conditions with seeing $\sim 0.6 - 1''$. The exposure on HD 4113 C were followed by a swap on a binary calibrator HD 25535 (Nowak et al. 2024a) and reduced using the standard exoGravity tools³ (GRAVITY Collaboration et al. 2020c). We used long exposure DIT=100 s to maximize the S/N. In about 1.7 h integration time on-target, we obtain an astrometry accuracy of about $\sim 50 - 100\text{ }\mu\text{as}$. We measure the spectrum of HD 4113 C with $R \sim 500$, showing a strong methane absorption band from $2.1\text{ }\mu\text{m}$ to $2.45\text{ }\mu\text{m}$. The typical sensitivity obtained of HD 4113 C in 1.7 h observations is comparable to the sensitivity obtained on 51 Eri in 5.4 h observations, as shown in Fig. 12, which illustrates the major improvement in the S/N between MACAO and GPAO. From previous observations, HD 4113 C has an estimated effective temperature $T \sim 500 - 600\text{ K}$ and a surface gravity $\log g = 5$ (Cheetham et al.

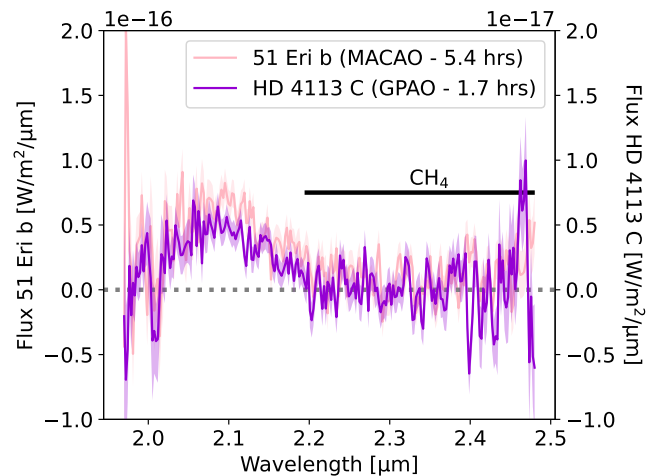


Fig. 12. GRAVITY off-axis spectrum of the brown dwarf companion HD 4113 C obtained with the new GPAO system compared to the off-axis spectrum of the exoplanet 51 Eri b obtained with the old MACAO system. We note the two different y-axes for the two objects, which show that a spectrum with a similar S/N can now be obtained for an approximately ten times fainter object.

2018). Its effective temperature is in tension with the isochronal mass estimate of $\sim 36\text{ M}_{\text{Jup}}$, making this target a potential binary brown dwarf candidate, as recently demonstrated in Gl229 B using GRAVITY resolving power (Xuan et al. 2024).

5.3.3. Mid-infrared L+M spectroscopy

The planet β Pictoris b (HD 39060 b) was observed with GPAO and MATISSE, using the GRA4MAT mode (Wollez et al. 2024). The observations were carried out during the night of 17 November 2024, with typical seeing conditions of $\sim 0.6''$. The MATISSE observations were obtained in L/M bands (Lopez et al. 2022), using the MEDIUM spectral resolution $R \sim 500$. From the coherent flux, the spectrum of β Pic b was extracted, following the methodology described in Houle et al. (2025). Figure 13 shows a comparison of the new spectrum obtained with the help of GPAO with that obtained with the help of MACAO extracted in the same way. We find that the MATISSE/MACAO

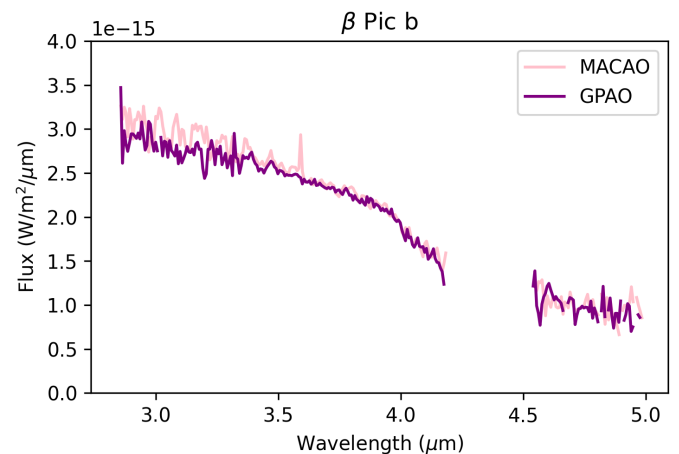


Fig. 13. Spectrum of β Pic b in the L and M bands obtained with MATISSE using MACAO and GPAO scaled by a factor of 4/3.

³ <https://gitlab.obspm.fr/mnowak/exogravity>

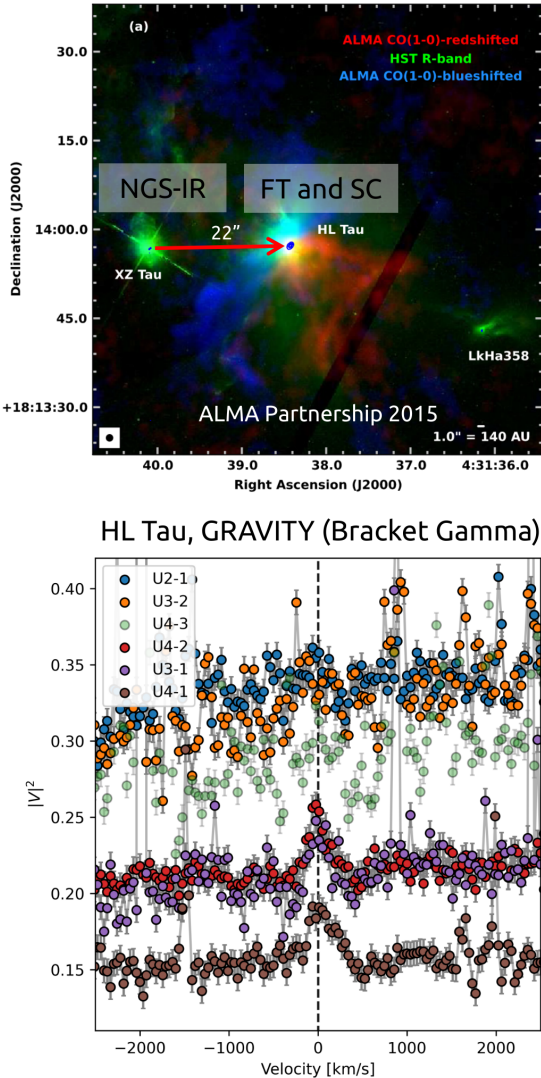


Fig. 14. Upper panel: Overview of the HL Tau region with ALMA and HST, adapted from [ALMA Partnership et al. \(2015\)](#). The NGS IR WFS was used on XZ Tau located at 22'' for the AO loop, while fringe-tracking and science was done on HL Tau with GRAVITY. **Lower panel:** Squared visibility of HL Tau, centered around the Br- γ line at 2.16 μ m.

spectrum is scaled by a factor $\approx 4/3$ (+30%) compared to the MATISSE/GPAO one. This means that, in the MACAO observation, either the flux of the star is underestimated or the flux of the planet is overestimated; or vice-versa in the GPAO observation. MATISSE uses spatial filtering, and the GRA4MAT narrow off-axis mode was still in development at the moment of the MACAO observation, with visible drifts in the data. Nevertheless, the comparison of both spectra show the GPAO one has a 20% higher S/N compared to the MACAO one in the same amount of time spent on source.

5.4. Embedded young stellar objects

The study of the inner astronomical unit of young stellar objects has advanced significantly thanks to infrared interferometry ([Lazareff et al. 2017](#); [GRAVITY Collaboration et al. 2019d](#); [Benisty et al. 2023](#)), but was essentially limited to Class II objects. This limitation originates from the extinction of the envelope surrounding these systems, which are bright in the K band but faint in the G band. The GPAO-LGS mode removes this limitation on the color of the AO target, making accessible Class I and T Tauri stars on statistical scale. The NGS IR mode enables these observations as well, in the specific case where a bright star in the K-band is located in the vicinity of the science target ($\sim 20''$).

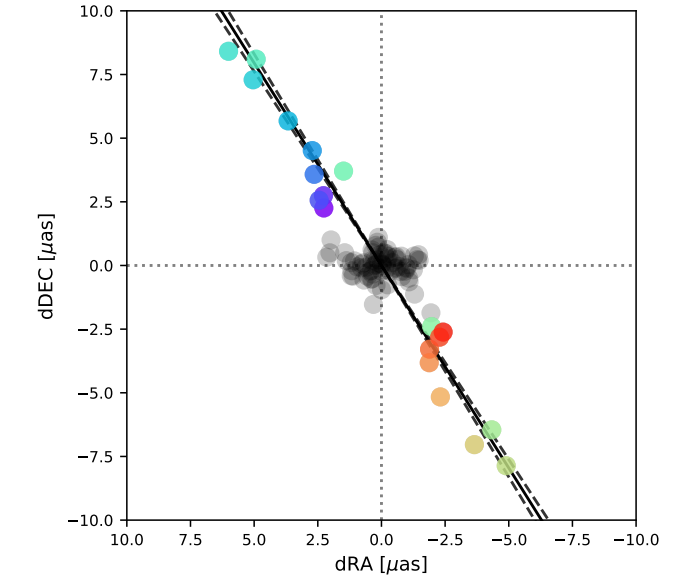


Fig. 15. Spectro-astrometry across the photospheric Br- γ absorption line of the star β Pictoris. Blue to red colours represent the velocity channels from -400 to $+400$ km s^{-1} . The gray points are the velocity channels in the continuum. The solid line is the best fit position angle for the rotation, with its uncertainty in dashed lines.

We used GPAO in the NGS_{IR} and GRAVITY to observe the protoplanetary disk in HL Tau. HL Tau is a T Tauri star ($M = 1.7 M_{\odot}$), located in Taurus ($d = 147$ pc). This system has been a prime target of sub-millimetric interferometry and ALMA ([ALMA Partnership et al. 2015](#)), but was never observed with VLTI due to its extremely red color ($m_R - m_K = 7.0$). The GRAVITY observations were performed by closing the NGS_{IR} WFS loop on the nearby star XZ Tau ($m_H = 8.15$), located at a separation of 22.5''. HL Tau was observed on 14 December 2024, with 30 min integration on source and a typical seeing 0.5 – 0.7''. The observations were carried out at a high-spectral resolution $R \sim 4000$, which also allows spectro-astrometry of Br- γ to be obtained.

In the continuum, the visibility amplitudes show that the inner disk of HL Tau is spatially resolved with GRAVITY, with visibility amplitudes smaller than 1 and consistently decreasing for the longer baselines U1-U4, U2-U3. The preliminary fit of the GRAVITY data converges to a typical half-radius of $a \sim 2.0$ mas, which is consistent with the values extrapolated from T Tauri stars ([GRAVITY Collaboration et al. 2021](#)). In addition, the differential amplitudes in Br- γ (Fig. 14, lower panel) show that the magnetospheric region in this star is resolved. The differential spectro-astrometry provides a typical precision of < 1 deg in HL Tau, which makes it possible to probe the kinematics of Br- γ in the magnetospheric region. The visibility amplitude also includes a significant contribution of extended flux as probed on the short baseline U1-U2 and U3-U2. This halo corresponds to an envelope in Class I objects, which can be seen for this object on the GRAVITY Acquisition Camera (not shown

here) and on near-infrared and ALMA images (Fig. 14, upper panel). These observations are the first resolved observations of the inner disk of HL Tau below the astronomical scale unit and the first resolved observations of its magnetospheric accretion region. The detailed analysis of these data is beyond the scope of this paper and will be presented in an upcoming publication.

These observations demonstrate the feasibility of studying T Tauri stars and Class I objects with GRAVITY+. This will be greatly generalized with GPAO-LGS, which will enable virtually the whole population of T Tauri stars to be covered.

5.5. Sub-micro-arcsecond spectro-astrometry

We illustrate the performance on bright targets with data recorded on the star β Pictoris (HD 39060). This star was used as a reference during an observation of the planet β Pic b, for a total integration time on the star of 6 min. We analyzed the data following the same methodology as Le Bouquin et al. (2009), later applied on β Pictoris (Kraus et al. 2020). Figure 15 shows the resulting spectro-astrometric signal across the photospheric Br- γ absorption line. The rotation of the photosphere is very well resolved, with a spectro-astrometric precision of 0.6 mas ($1-\sigma$) per spectral channel at $R \approx 4000$. From our record, this is the first measurement with sub-micro arcsecond precision in the optical. Thanks to this exquisite precision, the position angle of the stellar rotation axis is pinned down to 32.09 ± 0.9 deg (east of north). It allows us to answer a long standing question in this system: the stellar rotation is better aligned with the inner warped secondary disk close to the star, oriented along 33.3 ± 0.6 deg, rather than with the extended primary disk, oriented along 29.3 ± 0.3 deg (Lagrange et al. 2012).

6. Conclusion and prospects

This paper presents the design and implementation of the GRAVITY Plus Adaptive Optics for the VLTI, which introduces an extreme AO (NGS mode) and a faint AO (LGS mode) capability to optical interferometry for the first time. This paper demonstrates the performance obtained with extreme AO, which achieves fringe-tracking up to magnitude $m_K = 12.5$, wide-field fringe-tracking, spectroscopy on $m_K \approx 21$ substellar objects with $R = 500$, an improvement of a factor of 10 in sensitivity on exoplanet observations, sub-micro arcsecond spectro-astrometry, and fringe-tracking residuals ≈ 100 nm on the UTs for bright targets.

GPAO-NGS will be the workhorse of the VLTI high-contrast mode for exoplanet observations in the years to come. In terms of future research, the first avenue is the implementation of wavefront control and so-called dark-hole techniques (Pourré et al. 2022, 2024). This method consists in injecting modal offsets into the AO to null the starlight at the exact location of the SC fiber. The improvement will benefit particularly short-separation planets with 10^{-6} contrast at ≈ 100 mas. This range of separation is particularly synergistic with the discovery space of Gaia DR4. Even further, the GPAO-NGS will be essential for possible upgrades of VLTI to shorter wavelengths in the J band, by upgrading the system to 1.5 kHz and 900 corrected KL modes. Additional prospects include the recommissioning of secondary guiding between the Coudé focus and the interferometric laboratory (Pfuhl et al. 2014) to correct for the VLTI tunnel turbulence.

The deployment of the laser guide stars on all UTs in at the end of 2025 (Gravity+ Collaboration et al. 2022; Booth et al. 2024) will provide the complete implementation of GPAO. The

GPAO-LGS mode will make it possible to perform AO correction up to magnitude $G_{RP} \approx 17$ with a visible tip-tilt star or up to $m_K \approx 12$ with an infrared tip-tilt star. Combined with the wide-field fringe-tracking capability, the LGS mode will immediately increase the sky coverage available at VLTI by two orders of magnitude. For future research, the design of the low-order NGS wavefront sensors of GPAO-LGS enables many more modes than tip, tilt, and focus to be controlled (up to 12 modes in LO VIS and up to 44 in LO IR). The pros (reduced cone effect) and cons (added measurement noise) of increasing this number of modes will be explored. This is especially promising for the characterization of exoplanets around embedded young stars.

The combined GRAVITY+ upgrades bring VLTI UTs to a limiting magnitude of $m_K \approx 21$ (1h integration time in medium spectral resolution, under optimal conditions). This is getting close to the fundamental background limit that stands at $m_K \approx 25$ (see Appendix G). The worst offender is the transmission, which is shared equally between the infrastructure and the instrument. The tracking limit at $m_K \approx 12.5$ still falls far short from its fundamental quantum limit of $m_K \approx 20$, with a supplementary offender being the vibrations of the infrastructure.

To conclude, the upgrade of VLTI with extreme AO and the upcoming deployment of the LGS mode is a true paradigm shift for observations of the optical Universe at very high angular resolution. It opens up a new parameter space for the spatially resolved study of the Galactic Center, extragalactic science at high and low redshift, exoplanets at high-contrast, the inner region of protoplanetary disks, and more cases that are yet to be unveiled. With the synergy between LGS-assisted, high performance AO and interferometry, the Paranal Very Large Telescope is reaching the most advanced vision of its initial founders (see the *VLT Blue Book*⁴, 1987). The time has come to imagine what could be the next vision for spatially resolved, high sensitivity, and high contrast optical astronomy.

Acknowledgements. We are very grateful to our funding agencies (MPG, ERC, CNRS [PNCG, PNGRAM], ANR [contracts: AGN Melba ANR-21-CE31-0011, ExoVLTI ANR-21-CE31-0017], European Union’s Horizon 2020 research and innovation programme [grant agreements: ORP RadioNet Pilot - No 101004719, SCIFY - No 866070, UniverScale - No 951549], DFG, BMBF, Paris Observatory [CS, PhyFOG], Observatoire des Sciences de l’Univers de Grenoble, Université Grenoble Alpes, Observatoire de la Côte d’Azur, Université Côte d’Azur, Région Sud, Fundação para a Ciência e Tecnologia, the Science Foundation Ireland [Grant No. 18/SIRG/5597], the Research Foundation - Flanders (FWO) [Grant No. 1234224N], Région Auvergne-Rhône-Alpes, and the generous support from the Max Planck Foundation - an independent, non profit organization of private supporters of top research in the Max Planck Society. JBLB thanks E. Gendron and Y. Clenet. F.M would like to thank L. Perez. The community is encouraged to prepare their future VLTI observations with the dedicated tools developed by the JMMC, in particular `searchfft`⁵, `aspro2`⁶ and `searchCal`⁷, which were also used in this work. This research made use of the SIMBAD database, operated at CDS, Strasbourg, France. This work made use of `Astropy`⁸ a community-developed core Python package and an ecosystem of tools and resources for astronomy (Astropy Collaboration et al. 2013, 2018, 2022). We thank the anonymous referee for his comments, which helped improve this article. We express our sincere gratitude to the operational staff at ESO/Paranal and ESO, as well as the scientific, administrative, and technical staff at our institutions, who have made GPAO a reality.

References

Abuter, R., Allouche, F., Amorim, A., et al. 2024, *Nature*, 627, 281

⁴ https://www.eso.org/public/products/books/book_0005

⁵ <https://searchft.jmmc.fr>

⁶ <https://www.jmmc.fr/aspro>

⁷ <https://www.jmmc.fr/searchcal>

⁸ <https://www.astropy.org/>

Agapito, G., Pinna, E., Puglisi, A., & Rossi, F. 2019, AO4ELT6 proceedings, arXiv:1911.05989

ALMA Partnership, Brogan, C. L., Pérez, L. M., et al. 2015, *ApJ*, 808, L3

Arsenault, R., Alonso, J., Bonnet, H., et al. 2003, in Society of Photo-Optical Instrumentation Engineers (SPIE) Conference Series, Vol. 4839, Adaptive Optical System Technologies II, ed. P. L. Wizinowich & D. Bonaccini, 174–185

Arsenault, R., Donaldson, R., Dupuy, C., et al. 2004, in Society of Photo-Optical Instrumentation Engineers (SPIE) Conference Series, Vol. 5490, Advancements in Adaptive Optics, ed. D. Bonaccini Calia, B. L. Ellerbroek, & R. Ragazzoni, 47–58

Baruffolo, A., Salasnich, B., Puglisi, A., et al. 2018, in Society of Photo-Optical Instrumentation Engineers (SPIE) Conference Series, Vol. 10707, Software and Cyberinfrastructure for Astronomy V, ed. J. C. Guzman & J. Ibsen, 107071H

Béchet, C., Tallon, M., & Thiébaut, É. 2012, in Society of Photo-Optical Instrumentation Engineers (SPIE) Conference Series, Vol. 8447, Adaptive Optics Systems III, ed. B. L. Ellerbroek, E. Marchetti, & J.-P. Véran, 84472C

Beckers, J. M. 1990, *The Messenger*, 60, 1

Benisty, M., Dominik, C., Follette, K., et al. 2023, in Astronomical Society of the Pacific Conference Series, Vol. 534, Protostars and Planets VII, ed. S. Inutsuka, Y. Aikawa, T. Muto, K. Tomida, & M. Tamura, 605

Berdeu, A., Bonnet, H., Le Bouquin, J. B., et al. 2024a, *A&A*, 687, A157

Berdeu, A., Bonnet, H., Le Bouquin, J.-B., et al. 2024b, in Society of Photo-Optical Instrumentation Engineers (SPIE) Conference Series, Vol. 13097, Adaptive Optics Systems IX, ed. K. J. Jackson, D. Schmidt, & E. Vernet, 130970T

Bertrou-Cantou, A., Gendron, E., Rousset, G., et al. 2022, *A&A*, 658, A49

Beuzit, J. L., Vigan, A., Mouillet, D., et al. 2019, *A&A*, 631, A155

Bigioli, A., Courtney-Barrer, B., Abuter, R., et al. 2022, in Society of Photo-Optical Instrumentation Engineers (SPIE) Conference Series, Vol. 12183, Optical and Infrared Interferometry and Imaging VIII, ed. A. Mérard, S. Sallum, & J. Sanchez-Bermudez, 121831Z

Booth, M. T., Scherbarth, M., Gonté, F., et al. 2024, in Society of Photo-Optical Instrumentation Engineers (SPIE) Conference Series, Vol. 13096, Ground-based and Airborne Instrumentation for Astronomy X, ed. J. J. Bryant, K. Motohara, & J. R. D. Vernet, 130969A

Bourdarot, G., Eisenhauer, F., Şenol Yazıcı, et al. 2024, in Optical and Infrared Interferometry and Imaging IX, ed. J. Kammerer, S. Sallum, & J. Sanchez-Bermudez, Vol. 13095, International Society for Optics and Photonics (SPIE), 130950N

Calia, D. B., Hackenberg, W., Holzlöhner, R., Lewis, S., & Pfrommer, T. 2014, *Advanced Optical Technologies*, 3, 345

Cheetham, A., Ségransan, D., Peretti, S., et al. 2018, *A&A*, 614, A16

Crowther, P. A., Schnurr, O., Hirschi, R., et al. 2010, *MNRAS*, 408, 731

Davies, R., Absil, O., Agapito, G., et al. 2023, *A&A*, 674, A207

Dong, S., Mérard, A., Delplancke-Ströbèle, F., et al. 2019, *ApJ*, 871, 70

Eisenhauer, Bourdarot, & Widmann. 2023, in ESO Documentation, Vol. VLT-TRE-GRP-0020

Eisenhauer, F. 2019, in The Very Large Telescope in 2030, 30

Eisenhauer, F., Monnier, J. D., & Pfuhl, O. 2023, *ARA&A*, 61, 237

Fabricius, M., Woillez, J., Abuter, R., et al. 2024, in Society of Photo-Optical Instrumentation Engineers (SPIE) Conference Series, Vol. 13095, Optical and Infrared Interferometry and Imaging IX, ed. J. Kammerer, S. Sallum, & J. Sanchez-Bermudez, 130950B

Feast, M. W., Thackeray, A. D., & Wesselink, A. J. 1960, *MNRAS*, 121, 337

Fusco, T., Sauvage, J. F., Petit, C., et al. 2014, in Society of Photo-Optical Instrumentation Engineers (SPIE) Conference Series, Vol. 9148, Adaptive Optics Systems IV, ed. E. Marchetti, L. M. Close, & J.-P. Vran, 91481U

Gaia Collaboration, Brown, A. G. A., Vallenari, A., et al. 2021, *A&A*, 649, A1

Gitton, P. B., Leveque, S. A., Avila, G., & Phan Duc, T. 2004, in Society of Photo-Optical Instrumentation Engineers (SPIE) Conference Series, Vol. 5491, New Frontiers in Stellar Interferometry, ed. W. A. Traub, 944

GRAVITY Collaboration, Abuter, R., Accardo, M., et al. 2017, *A&A*, 602, A94

GRAVITY Collaboration, Abuter, R., Aimar, N., et al. 2022, *A&A*, 657, L12

Gravity+ Collaboration, Abuter, R., Alarcon, P., et al. 2022, *The Messenger*, 189, 17

GRAVITY+ Collaboration, Abuter, R., Allouche, F., et al. 2022, *A&A*, 665, A75

GRAVITY Collaboration, Abuter, R., Amorim, A., et al. 2018a, *A&A*, 615, L15

GRAVITY Collaboration, Abuter, R., Amorim, A., et al. 2020a, *A&A*, 636, L5

GRAVITY Collaboration, Abuter, R., Amorim, A., et al. 2018b, *A&A*, 618, L10

GRAVITY Collaboration, Abuter, R., Amorim, A., et al. 2019a, *A&A*, 625, L10

GRAVITY Collaboration, Amorim, A., Bourdarot, G., et al. 2024a, *A&A*, 684, A167

GRAVITY Collaboration, Garcia Lopez, R., Natta, A., et al. 2020b, *Nature*, 584, 547

GRAVITY Collaboration, Lacour, S., Nowak, M., et al. 2019b, *A&A*, 623, L11

GRAVITY Collaboration, Nowacki, H., Perraut, K., et al. 2024b, *A&A*, 690, A123

GRAVITY Collaboration, Nowak, M., Lacour, S., et al. 2020c, *A&A*, 633, A110

GRAVITY Collaboration, Perraut, K., Labadie, L., et al. 2021, *A&A*, 655, A73

GRAVITY Collaboration, Perraut, K., Labadie, L., et al. 2019c, *A&A*, 632, A53

GRAVITY Collaboration, Perraut, K., Labadie, L., et al. 2019d, *A&A*, 632, A53

GRAVITY Collaboration, Sturm, E., Dexter, J., et al. 2018c, *Nature*, 563, 657

GRAVITY Collaboration, Wojtczak, J. A., Labadie, L., et al. 2023, *A&A*, 669, A59

Hartke, J., Kakkad, D., Reyes, C., et al. 2020, in Society of Photo-Optical Instrumentation Engineers (SPIE) Conference Series, Vol. 11448, Adaptive Optics Systems VII, ed. L. Schreiber, D. Schmidt, & E. Vernet, 114480V

Herrier, C. T. 2019, *Video Memorie della Società Astronomica Italiana*, 1, 12

Herrier, C. T., Fusco, T., Oberti, S., et al. 2021, *MNRAS*, 504, 4274

Houle, M., Millour, F., Berio, P., et al. 2025, *A&A*, accepted

Karpov, V., Protopopov, V., Clements, W., et al. 2011, in Second International Conference on Adaptive Optics for Extremely Large Telescopes. Online at <http://ao4elt2.lesia.obspm.fr/>, 52

Kendrew, S., Hippler, S., Brandner, W., et al. 2012, in Ground-based and Airborne Instrumentation for Astronomy IV, ed. I. S. McLean, S. K. Ramsay, & H. Takami, Vol. 8446 (SPIE), 84467W

Kolb, J., Madec, P. Y., Le Louarn, M., Muller, N., & Béchet, C. 2012, in Society of Photo-Optical Instrumentation Engineers (SPIE) Conference Series, Vol. 8447, Adaptive Optics Systems III, ed. B. L. Ellerbroek, E. Marchetti, & J.-P. Véran, 84472D

Kraus, S., Le Bouquin, J.-B., Kreplin, A., et al. 2020, *ApJ*, 897, L8

Kraus, S., Mortimer, D., Chhabra, S., et al. 2022, in Society of Photo-Optical Instrumentation Engineers (SPIE) Conference Series, Vol. 12183, Optical and Infrared Interferometry and Imaging VIII, ed. A. Mérard, S. Sallum, & J. Sanchez-Bermudez, 121831S

Lacour, S. 2023, *Comptes Rendus. Physique*, 24, 115

Lacour, S., Carrión-González, Ó., & Nowak, M. 2025, *A&A*, 694, A277

Lacour, S., Wang, J. J., Rodet, L., et al. 2021, *A&A*, 654, L2

Lagrange, A. M., Boccaletti, A., Milli, J., et al. 2012, *A&A*, 542, A40

Laugier, R., Woillez, J., Defrère, D., et al. 2024, in Society of Photo-Optical Instrumentation Engineers (SPIE) Conference Series, Vol. 13095, Optical and Infrared Interferometry and Imaging IX, ed. J. Kammerer, S. Sallum, & J. Sanchez-Bermudez, 130950M

Lazareff, B., Berger, J. P., Kluska, J., et al. 2017, *A&A*, 599, A85

Le Bouquin, J. B., Absil, O., Benisty, M., et al. 2009, *A&A*, 498, L41

Le Bouquin, J.-B., Berger, J.-P., Beuzit, J.-L., et al. 2018, in Society of Photo-Optical Instrumentation Engineers (SPIE) Conference Series, Vol. 10703, Adaptive Optics Systems VI, ed. L. M. Close, L. Schreiber, & D. Schmidt, 1070371

Le Bouquin, J. B., Berger, J. P., Lazareff, B., et al. 2011, *A&A*, 535, A67

Léna, P. 1988, in European Southern Observatory Conference and Workshop Proceedings, Vol. 29, European Southern Observatory Conference and Workshop Proceedings, ed. F. Merkle, 899–908

Lopez, B., Lagarde, S., Petrov, R. G., et al. 2022, *A&A*, 659, A192

Maiolino, R., Risaliti, G., Signorini, M., et al. 2025, *MNRAS*, 538, 1921

Maiolino, R., Scholtz, J., Curtis-Lake, E., et al. 2024, *A&A*, 691, A145

Mérard, A. & Leibundgut, B. 2019, *The Messenger*, 177, 67

Milli, J., Kasper, M., Bourget, P., et al. 2018, in Society of Photo-Optical Instrumentation Engineers (SPIE) Conference Series, Vol. 10703, Adaptive Optics Systems VI, ed. L. M. Close, L. Schreiber, & D. Schmidt, 107032A

Millour, F., Bourdarot, G., Le Bouquin, J.-B., et al. 2024, in Society of Photo-Optical Instrumentation Engineers (SPIE) Conference Series, Vol. 13095, Optical and Infrared Interferometry and Imaging IX, ed. J. Kammerer, S. Sallum, & J. Sanchez-Bermudez, 1309520

Naidu, R. P., Matthee, J., Katz, H., et al. 2025, under review in *Nature*, arXiv:2503.16596

Nijenhuis, J., Kamphues, F., van Riel, M., et al. 2024, in Advances in Optical and Mechanical Technologies for Telescopes and Instrumentation VI, ed. R. Navarro & R. Jedamzik, Vol. 13100, International Society for Optics and Photonics (SPIE), 131001D

Nijenhuis, J. R. & Giesen, P. T. M. 2005, in Optomechanics 2005, ed. A. E. Hathaway, Vol. 5877, International Society for Optics and Photonics (SPIE), 587703

Nowak, M., Lacour, S., Abuter, R., et al. 2024a, *A&A*, 687, A248

Nowak, M., Lacour, S., Abuter, R., et al. 2024b, *A&A*, 684, A184

Nowak, M., Lacour, S., Lagrange, A. M., et al. 2020, *A&A*, 642, L2

Oberti, S., Quirós-Pacheco, F., Espósito, S., et al. 2006, in Society of Photo-Optical Instrumentation Engineers (SPIE) Conference Series, Vol. 6272, Advances in Adaptive Optics II, ed. B. L. Ellerbroek & D. Bonaccini Calia, 627220

Paufique, J., Madec, P.-Y., Kolb, J., et al. 2016, in Society of Photo-Optical Instrumentation Engineers (SPIE) Conference Series, Vol. 9909, Adaptive Optics Systems V, ed. E. Marchetti, L. M. Close, & J.-P. Véran, 99092H

Pfuhl, O., Haug, M., Eisenhauer, F., et al. 2014, in Society of Photo-Optical Instrumentation Engineers (SPIE) Conference Series, Vol. 9146, Optical and Infrared Interferometry IV, ed. J. K. Rajagopal, M. J. Creech-Eakman, & F. Malbet, 914623

Pourré, N., Le Bouquin, J.-B., Woillez, J., et al. 2022, in Society of Photo-Optical Instrumentation Engineers (SPIE) Conference Series, Vol. 12183, Optical and Infrared Interferometry and Imaging VIII, ed. A. Mérand, S. Sallum, & J. Sanchez-Bermudez, 121830V

Pourré, N., Winterhalder, T. O., Le Bouquin, J. B., et al. 2024, *A&A*, 686, A258

Pourré, N. 2024, PhD thesis, Univ. Grenoble Alpes, PhD Thesis, supervisors: Rousselet-Perraut, Karine ; Le Bouquin, Jean-Baptiste

Riccardi, A., Esposito, S., Agapito, G., et al. 2018, in Society of Photo-Optical Instrumentation Engineers (SPIE) Conference Series, Vol. 10703, Adaptive Optics Systems VI, ed. L. M. Close, L. Schreiber, & D. Schmidt, 1070303

Riello, M., De Angeli, F., Evans, D. W., et al. 2021, *A&A*, 649, A3

Roddier, F. 1981, *Progress in Optics*, 19, 281

Scheithauer, S., Brander, W., Deen, C., et al. 2016, in Society of Photo-Optical Instrumentation Engineers (SPIE) Conference Series, Vol. 9909, Adaptive Optics Systems V, ed. E. Marchetti, L. M. Close, & J.-P. Véran, 99092L

Shaklan, S. & Roddier, F. 1988, *Appl. Opt.*, 27, 2334

Shchekaturov, P. 2023, in RTC4AO Workshop

Ströbele, S., Arsenault, R., Bacon, R., et al. 2006, in Society of Photo-Optical Instrumentation Engineers (SPIE) Conference Series, Vol. 6272, Advances in Adaptive Optics II, ed. B. L. Ellerbroek & D. Bonaccini Calia, 62720B

Tatulli, E., Blind, N., Berger, J. P., Chelli, A., & Malbet, F. 2010, *A&A*, 524, A65

Widmann, F., Gillessen, S., Ott, T., et al. 2022, in Society of Photo-Optical Instrumentation Engineers (SPIE) Conference Series, Vol. 12183, Optical and Infrared Interferometry and Imaging VIII, ed. A. Mérand, S. Sallum, & J. Sanchez-Bermudez, 121830U

Woillez, J., Abad, J. A., Abuter, R., et al. 2019, *A&A*, 629, A41

Woillez, J., Abuter, R., Andolfato, L., et al. 2014, in Optical and Infrared Interferometry IV, ed. J. K. Rajagopal, M. J. Creech-Eakman, & F. Malbet, Vol. 9146, International Society for Optics and Photonics (SPIE), 91461H

Woillez, J., Petrov, R., Abuter, R., et al. 2024, *A&A*, 688, A190

Wolf, C., Lai, S., Onken, C. A., et al. 2024, *Nature Astronomy*, 8, 520

Xuan, J. W., Mérand, A., Thompson, W., et al. 2024, *Nature*, 634, 1070

²¹ School of Physics, University College Dublin, Dublin 4, Belfield, Ireland

²² Instituto de Astronomía, Universidad Nacional Autónoma de México, Apdo. Postal 70264, Ciudad de México 04510, Mexico

²³ Laboratoire Lagrange, Univ. Côte d'Azur, CNRS, OCA, Nice, France

²⁴ University of Lyon 1, ENS de Lyon, CNRS, Lyon, France

²⁵ Research School of Astronomy and Astrophysics, Australian National University, Canberra 2611, Australia

²⁶ Dublin Institute for Advanced Studies, 31 Fitzwilliam Place, D02 XF86 Dublin, Ireland

²⁷ French-Chilean Laboratory for Astronomy, IRL 3386, CNRS and U. de Chile, Casilla 36-D, Santiago, Chile

²⁸ The Kavli Institute for Astronomy and Astrophysics, Peking University, Beijing 100871, China

¹ Max Planck Institute for extraterrestrial Physics, Giessenbachstraße 1, 85748 Garching, Germany

² LIRA, Observatoire de Paris, Université PSL, Sorbonne Université, Université Paris Cité, CY Cergy Paris Université, CNRS, 92190 Meudon, France

³ Max Planck Institute for Astronomy, Königstuhl 17, 69117 Heidelberg, Germany

⁴ 1st Institute of Physics, University of Cologne, Zülpicher Straße 77, 50937 Cologne, Germany

⁵ Univ. Grenoble Alpes, CNRS, IPAG, 38000 Grenoble, France

⁶ Universidade de Lisboa - Faculdade de Ciências, Campo Grande, 1749-016 Lisboa, Portugal

⁷ Faculdade de Engenharia, Universidade do Porto, rua Dr. Roberto Frias, 4200-465 Porto, Portugal

⁸ European Southern Observatory, Karl-Schwarzschild-Straße 2, 85748 Garching, Germany

⁹ European Southern Observatory, Casilla 19001, Santiago 19, Chile

¹⁰ Sterrewacht Leiden, Leiden University, Postbus 9513, 2300 RA Leiden, The Netherlands

¹¹ Departments of Physics and Astronomy, Le Conte Hall, University of California, Berkeley, CA 94720, USA

¹² CENTRA - Centro de Astrofísica e Gravitação, IST, Universidade de Lisboa, 1049-001 Lisboa, Portugal

¹³ Department of Physics, Technical University Munich, James-Franck-Straße 1, 85748 Garching, Germany

¹⁴ Max Planck Institute for Radio Astronomy, Auf dem Hügel 69, 53121 Bonn, Germany

¹⁵ Department of Physics, University of Illinois, 1110 West Green Street, Urbana, IL 61801, USA

¹⁶ Hamburger Sternwarte, Universität Hamburg, Gojenbergsweg 112, 21029 Hamburg, Germany

¹⁷ School of Physics & Astronomy, University of Southampton, Southampton, SO17 1BJ, United Kingdom

¹⁸ Center for Astrophysics | Harvard & Smithsonian, 60 Garden Street, Cambridge, MA, 02138, USA

¹⁹ Max Planck Institute for Astrophysics, Karl-Schwarzschild-Straße 1, 85741 Garching, Germany

²⁰ Institute of Astronomy, KU Leuven, Celestijnenlaan 200D, B-3001, Leuven, Belgium

Appendix A: Conceptual differences with ERIS

Although GPAO shares a large number of requirements and constraints with ERIS and AOF, there is a set of differences with significant impact on the design choices and development strategy. (I) The DM of GPAO does not have an absolute feedback position sensor. The actual DM shape can only be inferred from the command vector sent to the DM. (II) In GPAO, the DM (located in M8) and the photometric pupil (located in M2) are two different optical surfaces, linked with a variable wobble and rotation angle (the elevation). (III) GPAO has access to the Nasmyth beacon of the Unit Telescope, located before the DM (near M4). It allows closed loop tests and calibration of the AO during daytime. ERIS and the AOF instruments do not have access to this tool: AO calibrations and tests can only be executed at night, on star light. (IV) GPAO only has a loose requirement regarding the absolute position and the slow drift of the field sent to the science instrument ($< 0.2''$ for GPAO with respect to $< 0.01''$ for ERIS). Indeed, the VLTI provides a secondary tip-tilt guiding to GPAO, at a rate of 1 Hz, ensuring a constant fine alignment of the field. (V) Interferometric fringe tracking requires a diffraction-limited beam, at least partially. The disappearance of a coherent core in the delivered PSF corresponds to the practical limiting magnitude. Therefore, there is no such modes as “seeing enhancer” (only LGS correction) or “seeing limited” (no AO correction) in GPAO.

Appendix B: Parameters of the PSIM model

Table B.1 sums up the parameters of the PSIM model of the different GPAOs, namely (i) the DM amplitude, and (ii) the DM/WFS mis-registration parameters: the DM pattern magnification and anamorphoses (along the 0 deg and 45 deg axes) on the WFS and the offset angle between the DM and the WFS (the actual angle between the DM and WFS evolving with the azimuth az). All these parameters were fitted on the UT Nasmyth beacon. The on-sky photometric pupil scale is not a PSIM parameter but is indicated for information. For the LGS WFS, it is yet to be measured on-sky for GPAO1-2-3. The magnification of the photometric pupil in the NGS IR WFS is not fitted due to the lack of sensitivity of the 9×9 SH-WFS.

Appendix C: Secondary loops

The Secondary Loops (SL) run in the OS software, typically at a period of a few seconds. The function of most of them has already been introduced in Sect. 3.4. We provide here a simple but exhaustive summary.

SL1 offloads the DM shape in the active optics of the M1 mirror of the UT. This loop has been decommissioned because the DM has enough stroke.

SL2 guides the DM registration on the NGS VIS WFS using the NPSM.

SL3 guides the DM registration on the LGS WFS, using the LPSM.

SL4 calculates the NCPA modal vector and reference slopes to be sent to the SRTC. The NCPA vector contains a static part and,

when observing off-axis, a dynamical part related to the aberrations across the M9 DIC and PBS.

SL5 updates the rotation angles of the PSIM model in the SRTC, which triggers the recomputation of the Control Matrices. It also updates the rotation angles of various monitoring components.

SL6 guides the DM registration on the NGS IR WFS using the Variable Curvature Mirror (VCM) of the STS.

SL7 offloads the focus measured in the LGS WFS into the LFOC device.

SL8 offloads the mean tip and tilt components of the DM shape. The offload goes to the telescope axes when observing on-sky or goes to the QSM when using the Nasmyth beacon.

SL9 implements the pointing model and the tracking trajectory for the laser Jitter Mirror, by regularly updating the SRTC. Doing so, it ensures that the laser spot remains inside the LGS WFS even when the Jitter loop is open.

Appendix D: Data flow of the HRTC

Figure D.1 presents a simplified diagram of the data flow in the GPAO HRTC. The high-order controllers are implemented as “implicitly modal”: the input slope vector is converted into a delta-command vector in DM space by the matrix multiplication with the Control Matrix. These delta-commands are filtered by a temporal IIR filter, identical for all elements of the delta-command vector (as-of-now, the IIR is configured as a pure integrator). On the other hand, the low order controllers are implemented as “explicitly modal”: the temporal IIR filter acts on the delta-command expressed in KL modes. The IIR filter is possibly different for each mode. A second matrix multiplication then projects the modes into the DM actuator space.

If needed, the commands from the low order and the high-order pipelines are summed. The output command vector is clipped to $+1/-1$, in unit of DM maximum stroke. The total power of the command ($\sum c_i^2$) is compared to the maximum power allowed by the DM electronic, and if larger, the command is not sent to the DM and the IIR filter is frozen. Clipping (e.g. zonal saturation) regularly occurs on a few actuators on the edges when the seeing goes above $1.5''$. Freezing (e.g., power saturation) only occurs in pathological cases such as a wrong alignment. Note that clipping a few actuators has a negligible impact on the delivered image quality, but freezing the command is generally dramatic.

GPAO implements the classical anti-windup method: the clipped part of the command vector (if any) is subtracted to the delta-command of the next loop-cycle. It prevents from large accumulation of uncorrected commands inside the controller (“windup”), which would take a long time to reset when the disturbance actually comes back inside the dynamic range. Simulations demonstrated the importance of this anti-windup path.

GPAO also implements an innovative modal leak path: the command actually sent to the DM is filtered through a leak matrix and subtracted to the delta-command of the next loop-cycle. This leak matrix is constructed in a way to (1) fully leak the uncontrolled space and (2) partially leak the high-order controlled

Table B.1. Parameters of the PSIM model for the four GPAOs.

Parameter	Description	Unit	GPAO1	GPAO2	GPAO3	GPAO4
COMMON						
DM inclination	design	deg	13.26	13.26	13.26	13.26
DM stroke ^a	measured	μm	3.9	3.7	3.8	3.9
NGS VIS (measured in HO 40 × 40)						
DM/WFS pitch scaling	measured	%	102.8	103.5	102.1	103.5
DM/WFS registration angle	az-12.984+	deg	0.60	1.21	-1.14	-2.95
DM/WFS anamorphosis ^b 0	measured	%	0	0	0	0
DM/WFS anamorphosis ^b 45	measured	%	0	0	0	0
Photometric pupil scale	measured	%	97.0	96.9	96.8	97.1
LGS						
DM/WFS pitch scaling	measured	%	101.3	102.2	101.2	102.0
DM/WFS registration angle	az-12.984+	deg	-88.00	-91.74	-88.65	-88.35
DM/WFS anamorphosis 0	measured	%	-0.2	-0.1	-0.2	-0.2
DM/WFS anamorphosis 45	measured	%	0.1	0.0	0.1	0.0
Photometric pupil scale	measured	%	-	-	-	99.0
NGS IR						
DM/WFS pitch scaling	measured	%	96.4	95.4	101.1	97.7
DM/WFS registration angle	az-12.984+	deg	78.71	80.01	83.81	81.11
DM/WFS anamorphosis 0	measured	%	0.6	3.7	-0.4	0.3
DM/WFS anamorphosis 45	measured	%	0.6	-0.6	-0.8	0.0

Notes. ^(a) In PSIM, the DM stroke is defined as the maximum mechanical deformation of the surface when pushing a single actuator, with respect to the reference. This mechanical stroke is achievable toward the positive and toward the negative direction. ^(b) The anamorphoses of the NGS VIS wavefront sensor were measured to be negligible with a fixed offset and an azimuthal contributions below 0.04 % each. We consequently let them equal to 0% in the PSIM model.

modes. Mathematically, let's call $A2S$ the interaction matrix (actuators to slopes) and $M2A$ the modal matrix (modes to actuators). Let's call G_m a vector of modal gain, and L_m a vector of modal leak (typically 0 for the first modes and 0.5 for the highest controlled modes). Then, the high-order control matrix writes

$$CM = M2A \times G_m \times (A2S \times M2A)^{-1}, \quad (D.1)$$

and the leak matrix writes

$$LM = \mathbb{I} - M2A \times (\mathbb{I} - L_m) \times M2A^{-1}. \quad (D.2)$$

where \mathbb{I} is the identity matrix. The setup of the modal leak vector L_m in GPAO follows the prescriptions of [Agapito et al. \(2019\)](#). Note that the size of the high-order control matrix is $(N_{\text{slopes}} \times N_{\text{actuators}})$ while the size of the leak matrix is $(N_{\text{actuators}} \times N_{\text{actuators}})$. The computations of the anti-windup and of the leak paths are executed in the dead-time of the HRTC, that is once all computations depending on the pixels of the current frame are finished and before the pixels of the next frame arrive. Thus, these computations do not contribute to the overall latency.

The anti-windup does not contain any projection, and thus creates signal outside the control space, often called “garbage”. Nevertheless, there is no need for a dedicated garbage collector as in SPHERE ([Fusco et al. 2014](#)) because the uncontrolled space is quickly erased by the LM projection at frame rate.

Appendix E: Transmission

Figure E.1 and Figure E.2 show the total number of electrons received on the detector of the visible WFS and of the infrared WFS as a function of the Gaia red-pass (G_{RP}) or K-band magnitude of the guide star. The figures include all science observations from December 2024 to February 2025. We consider a detector conversion gain of 30 e/adu for the OCAM2 camera and 10 e/adu for the Saphira IR detector. The measurements are corrected for the amplification gain and framerate.

Appendix F: Transfer function

The DM is modeled with a sum of 3 second-order resonances with frequencies $s_i = \{1055, 1265, 1600\}$ Hz, damping coefficients $\zeta_i = \{0.025, 0.025, 0.1\}$ and amplitudes $a_i = \{0.33, 0.4, 0.27\}$:

$$DM(s) = \sum_i \frac{a_i}{(\frac{s}{s_i})^2 + 2\zeta_i \frac{s}{s_i} + 1} \quad (F.1)$$

The WFS is modeled as a discrete integration window of integration time T_i :

$$WFS(s) = \frac{1 - e^{-sT_i}}{sT_i} \quad (F.2)$$

The controller is modeled as a discrete integrator with gain K_I and frame period T_c :

$$C(s) = \frac{K_I}{1 - e^{-sT_c}} \quad (F.3)$$

The output command is hold for one frame period T_c resulting in an additional:

$$H(s) = \frac{1 - e^{-sT_c}}{sT_c} \quad (F.4)$$

All other delays are factorized into a pure-delay T_d :

$$D(s) = e^{-sT_d} \quad (F.5)$$

The closed-loop rejection function writes:

$$R(s) = 1/(1 + DM(s).WFS(s).C(s).H(s).D(s)). \quad (F.6)$$

Measurements (dots) and models (lines) for the wavefront transfer function are presented in Fig. F.1. Leaks were deactivated during these measurements.

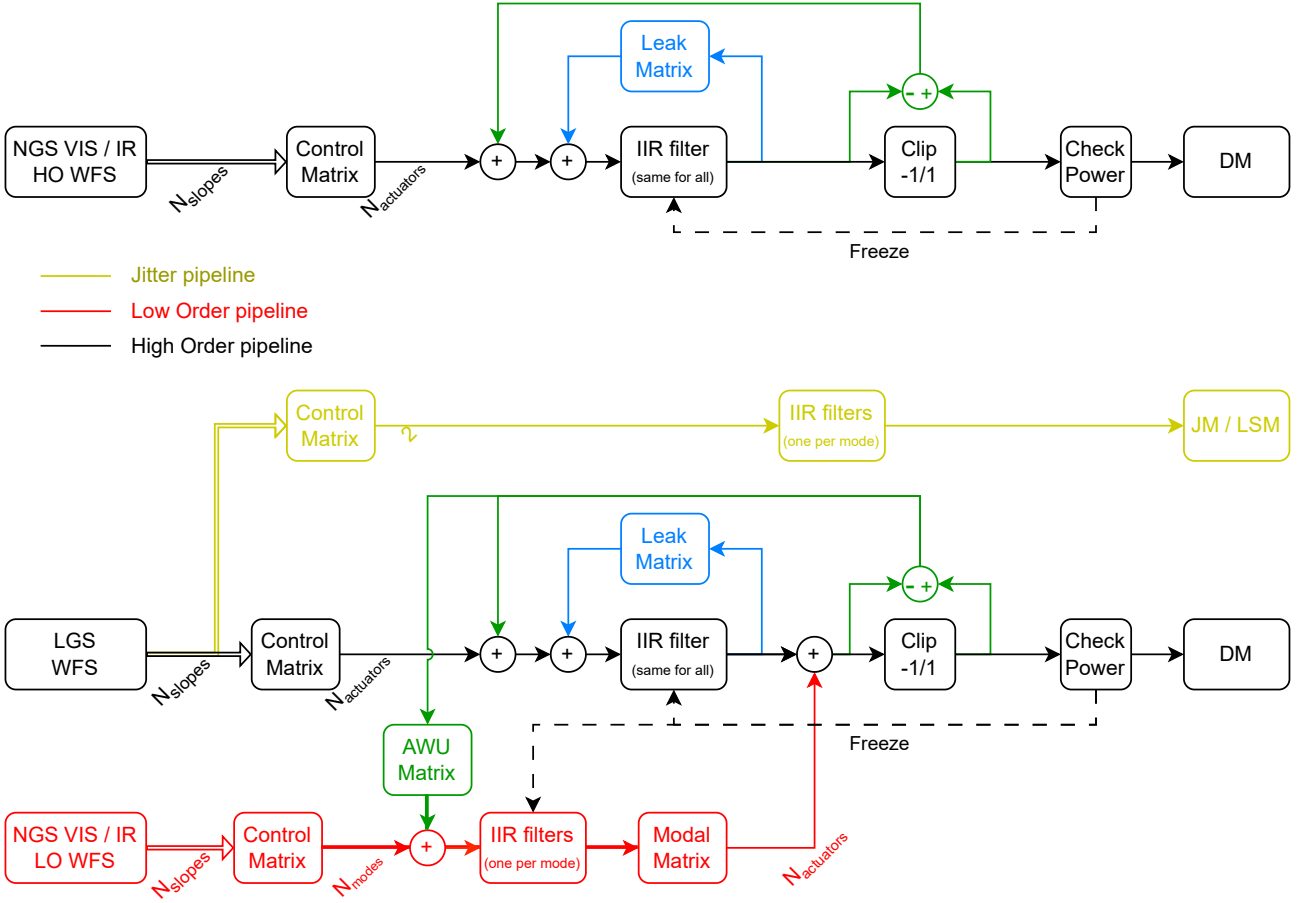


Fig. D.1. Simplified diagram of the real-time data-flow within the HRTC of GPAO when configured in NGS_VIS/IR mode (top) and in LGS_VIS/IR mode (bottom), from the slopes vectors computed by the Wavefront Sensors to the command vectors sent to the Deformable Mirror and to the Jitter Mirror. The black path is the HO pipeline, the red path is the LO pipeline, the yellow path is the Jitter pipeline. Each pipeline can be closed independently. The green feedback is the anti-windup and the blue feedback is the modal leak (which also acts as a garbage collector). To ease the reading, the diagram does not include the pre-processing from detector images to slopes, it does not include the reference slopes offsets, and it does not include the real-time disturbances (in slopes and command spaces) than can be input to the data-flow for calibration purposes.

Appendix G: Fundamental limits

This appendix recall the fundamental limits for correcting the atmosphere and integrating on the science. More details can be found in Eisenhauer et al. (2023). By "fundamental" we call limits that cannot be lifted by technological improvements (atmosphere characteristics, quantum noise, integration time). We restrict this example to the K-band for concision. The photon flux in $[\gamma \text{ m}^{-2} \text{ s}^{-1}]$ is estimated with the relation $n_\gamma = 10^{(25.0 - G_{\text{RP}})/2.5}$ in the visible and $n_\gamma = 10^{(23.4 - m_K)/2.5}$ in the infrared. We define a S/N of 5 as threshold for the limiting magnitude, so about 25 photons when quantum noise limited. We consider a turbulence with a Fried parameter $r_0 = 20 \text{ cm}$ and a coherence time of $\tau_0 = 10 \text{ ms}$ in the visible, and a longer coherence time of $\tau_0 = 40 \text{ ms}$ in the infrared. We consider a scientific integration time $T = 1 \text{ h}$. The infrared sky background is $m_K \approx 21$ for a solid angle of 40 mas^2 (acceptance of the GRAVITY single mode fiber, fixed by the 8 m diameter of the UTs).

NGS AO limit The NGS adaptive optics is limited by the S/N within the coherence volume defined by $r_0^2 \times \tau_0$. Getting 25 photons per volume translates into a magnitude $G_{\text{RP}} = 13.1$.

LGS-assisted AO limit The LGS-assisted adaptive optics is limited by the S/N within the coherence volume defined by $D^2 \times \tau_0$, where D is the diameter of the telescope. Getting 25 photons per volume translates into a magnitude $G_{\text{RP}} = 20.3$ for a 8 m aperture.

Fringe-tracking limit The fringe-tracking is limited by the S/N within the coherence volume defined by $\frac{2}{3}D^2 \times \tau_0$ (the fringe receives the flux of 2 telescopes, each of them being split in 3 to feed all pairs). Getting 25 photons per volume translates into a magnitude $m_K = 20.2$ for an array of four 8 m apertures.

Science limit At its best sensitivity in the lowest spectral resolution, the science is limited by the S/N within the coherence volume defined by $\frac{2}{3}D^2 \times T$. This is limited by the sky-background and not the quantum noise. Getting a number of photons equal to

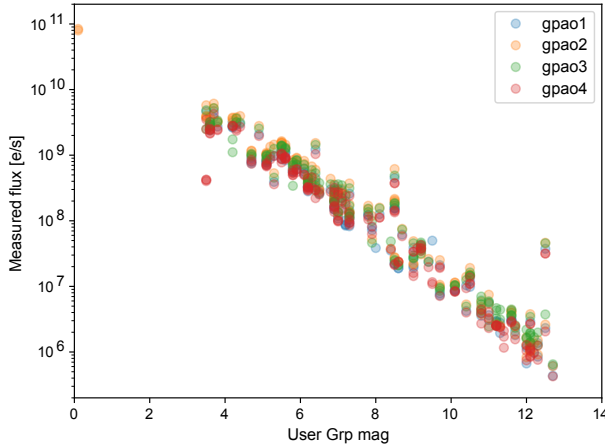


Fig. E.1. Measured total flux on the visible WFS of GPAO versus the G_{RP} Gaia magnitude.

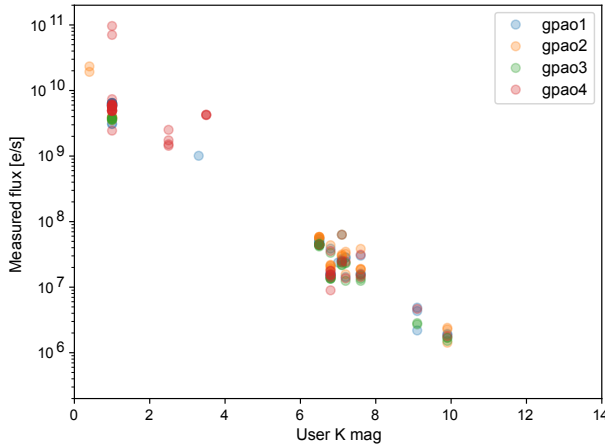


Fig. E.2. Measured total flux on the infrared NGS IR WFS versus the K band magnitude.

5 times the background photon noise translates into a magnitude $m_K = 25.2$ for an array of 8 m apertures.

Caveats This analysis has two caveats. First, the spatial filtering effect across the telescope aperture increases the coherence time of the piston. Secondly, the dilution factor $\frac{2}{3}$ is partially lifted by the global retrieval of all pistons with all measurements. As such, the above computed fringe-tracking limit is underestimated.

Appendix H: Nomenclature

2D	Two dimensional
ADC	Atmospheric Dispersion Compensator, made of 2 rotating prisms.
AGN	Active Galactic Nucleus
AO	Adaptive Optics
AOF	Adaptive Optics Facility
BLR	Broad Line Region
CCD	Charge Couple Device
CIAO	Coudé Infrared Adaptive Optics

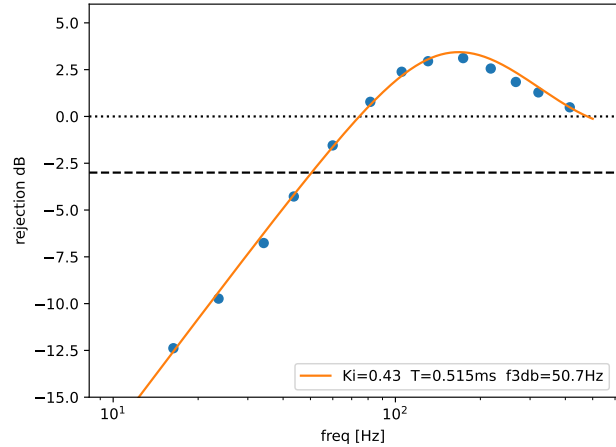


Fig. F.1. Measurements (dots) and models (lines) for the wavefront transfer function for the infrared (top) and visible WFS (bottom), configured at the maximum frame rate of 1000 Hz. The model is fitted to the data by adjusting the integral gain K_i and the pure-delay T_d . The rejection bandwidth defined at -3 dB is also given. Data are presented for GPAO2 but similar results are obtained on the other systems.

CM	Control Matrix
CO	Corrective Optics assembly, hosting the QSM and the DM, located in the M8 of the UT
Coudé	Train of mirrors M4 to M8 of the UT, co-rotating with azimuth
DCS	Detector Control Software
DM	Deformable Mirror
DCR	Dichroic splitting the blue (reflected toward the technical camera) and the red (transmitted toward the NGS WFS camera).
EMCCD	Electron-Multiplication Charge Coupled Device is a technology of fast and low noise visible camera
ERIS	Enhanced Resolution Imager and Spectrograph
ESO	European Southern Observatory
FT	Fringe Tracker
FSM	Field Steering Mirror of the STS, actuates the tip-tilt
GALACSI	Ground Atmospheric Layer Adaptive Corrector for Spectroscopic Imaging

GbE	Gigabit Ethernet	NCPA	Non common path aberrations, differential optical aberrations between the AO path and the scientific path.
GPAO	GRAVITY Plus Adaptive Optics	NDIA	NGS diaphragm, an adjustable field stop installed in the NGS VIS WFS.
GRAAL	GRound layer Adaptive optics Assisted by Lasers	NFB	Nasmyth Focus Beacon, a set of source at the folded Nasmyth focus of the UT, feeding toward the Coudé train.
G-Wide	GRAVITY-Wide is the new implementation of the dual beam, off-axis capability of VLTI allowing to feed the GRAVITY instrument with 2 fields separated by up to 1 arcmin.	NGS	Natural Guide Star
HO	High-order, in NGS modes and in opposition to the low-order in LGS modes.	NGS IR WFS	Infrared wavefront sensor on a natural guide star, the hardware is identical to the former CIAO WFS.
HSDL	High Speed Data Link	NGS VIS WFS	Visible wavefront sensor on a natural guide star. In the GPAO NGS_VIS mode, this corresponds to the 40×40 SH. In the GPAO LGS_VIS mode, this corresponds to the 4×4 SH.
HKL	House Keeping Link	NPSM	NGS Pupil Steering Mirror, located in a focal plan within the NGS VIS WFS
HRTC	Hard Real Time Computer, performs the real-time tasks	NROT	NGS derotator, fixed in operation
ICS	Instrument Control Software	OPD	Optical Path Difference
IF	Influence Functions	OS	Observation Software
IIR	Infinite Impulse Response is the default type of temporal filter used in SPARTA (alternative is PID).	PBS	Periscope Beam Splitter
IM	Interaction Matrix	PBS DIC	the Periscope Beam Splitter dichroic is the dichroic at the Coudé focus of the UT, splitting the LGS wavelength (reflected toward LGS WFS) and the broad band VIS (transmitted toward GPAO NGS VIS WFS)
IR	InfraRed	PID	Proportional Integral Derivative, a type of temporal filter.
IRIS	guiding camera of the VLTI	PIONIER	Precision Integrated-Optics Near-infrared Imaging ExpeRiment
ISS	The Interferometric Supervisor Software is the high-level layer coordinating the all the subsystems of VLTI.	PLC	Programmable Logic Controller, local controller to interface with the hardware, generally based on Beckhoff in the ESO context
JM	Jitter Mirror of the LGS Launch telescope, fast actuator to stabilize the observed position of the LGS spot in the WFS sensor.	PSM	Pupil Steering Mirror, lateral pupil actuator (LPSM in the LGS WFS, NPSM in the NGS WFS).
JWST	James Webb Space Telescope	QSM	Quasi Static Mount, gimbal tip-tilt mount of the DM, with slow motion and large steering range.
KL	Karhunen-Loé modes, in GPAO these modes are defined in DM command space.	RTC	Real Time Computer
LCU	Local Controller Unit, local controller to interface with the hardware, generally based on VXworks in the ESO context	SC	Science Channel
LFOC	Laser Focus Control, long range longitudinal motion of the entire LGS WFS assembly to maintain the focalisation toward the Sodium layer. The range extend toward infinity to allow observing the Nasmyth beacon of the UT	sFPDP	Serial Front Panel Data Port
LROT	LGS derotator, fixed in operation	SH	Shack-Hartmann wavefront sensor
LGS	Laser Guide Star	SL	Secondary Loop, supervision, or tracking, or guiding loop executed by the AOO process of the OS. Typical rate 1 to 10 s.
LO	Low order, in opposition to the high order in LGS modes	SMBH	Super Massive Black Hole
LPS	Laser Projection Subunit	S/N	Signal to noise ratio
LPSM	Laser Pupil Steering Mirror, located in a focal plan within the LGS WFS.	SPARTA	Standard Platform for Adaptive optics Real Time Applications, developed by ESO.
LSM	Laser Steering Mirror (called FSM in ERIS/AOF), slow offload actuator for the JM.	SPHERE	Spectro-Polarimetric High contrast imager for Exoplanets REsearch
M1	primary mirror of the UT, slowly deformable (active optics).	SRTC	Soft Real Time Computer, perform the supervision tasks
M2	secondary mirror, pupil stop of the UT.	STS	Star Separator, located in the VLT Coudé room, split the field-of-view into two region fed to the VLT
M9 DIC	Dichroic at the Coudé focus of the UT, splitting the IR (reflected toward STS) and the VIS (transmitted toward GPAO WFS).	UT	Unit Telescope.
MACAO	Multi-Application Curvature Adaptive Optics	VCM	Variable Curvature Mirror of the STS, also serving as lateral pupil actuator.
MATISSE	Multi AperTure mid-Infrared Spectro-Scopic Experiment	VIS	Visible
NAOMI	New Adaptive Optics Module for Interferometry, installed on the 1.8 m Auxiliary Telescopes of the VLTI.	VLT	Very Large Telescope.

VLTI Very Large Telescope Interferometer.

WFS WaveFront Sensor

XYT X,Y Table, 2D translation stage to patrol
the entire field-of-view at the Coudé focus
with the NGS WFS (NXYT) and with the
LGS WFS (LXYT)

YSO Young Stellar Object